



# Polar cap arcs from the magnetosphere to the ionosphere: kinetic modelling and observations by Cluster and TIMED

R. Maggiolo<sup>1</sup>, M. Echim<sup>1,2</sup>, C. Simon Wedlund<sup>1</sup>, Y. Zhang<sup>3</sup>, D. Fontaine<sup>4</sup>, G. Lointier<sup>5</sup>, and J.-G. Trotignon<sup>5</sup>

<sup>1</sup>Belgian Institute for Space Aeronomy (BIRA-IASB), Space Plasma, Brussels, Belgium

<sup>2</sup>Institute for Space Sciences, Bucharest, Romania

<sup>3</sup>The Johns Hopkins University Applied Physics Laboratory, Laurel, USA

<sup>4</sup>Laboratoire de Physique des Plasmas, Velizy, France

<sup>5</sup>LPCE/CNRS, Orléans, France

*Correspondence to:* R. Maggiolo (romain.maggiolo@aeronomie.be)

Received: 30 June 2011 – Revised: 18 October 2011 – Accepted: 19 December 2011 – Published: 3 February 2012

**Abstract.** On 1 April 2004 the GUVI imager onboard the TIMED spacecraft spots an isolated and elongated polar cap arc. About 20 min later, the Cluster satellites detect an isolated upflowing ion beam above the polar cap. Cluster observations show that the ions are accelerated upward by a quasi-stationary electric field. The field-aligned potential drop is estimated to about 700 V and the upflowing ions are accompanied by a tenuous population of isotropic protons with a temperature of about 500 eV.

The magnetic footpoints of the ion outflows observed by Cluster are situated in the prolongation of the polar cap arc observed by TIMED GUVI. The upflowing ion beam and the polar cap arc may be different signatures of the same phenomenon, as suggested by a recent statistical study of polar cap ion beams using Cluster data.

We use Cluster observations at high altitude as input to a quasi-stationary magnetosphere-ionosphere (MI) coupling model. Using a Knight-type current-voltage relationship and the current continuity at the topside ionosphere, the model computes the energy spectrum of precipitating electrons at the top of the ionosphere corresponding to the generator electric field observed by Cluster. The MI coupling model provides a field-aligned potential drop in agreement with Cluster observations of upflowing ions and a spatial scale of the polar cap arc consistent with the optical observations by TIMED. The computed energy spectrum of the precipitating electrons is used as input to the Trans4 ionospheric transport code. This 1-D model, based on Boltzmann's kinetic formalism, takes into account ionospheric processes such as photoionization and electron/proton precipitation, and computes the optical and UV emissions due to precipitating electrons. The

emission rates provided by the Trans4 code are compared to the optical observations by TIMED. They are similar in size and intensity. Data and modelling results are consistent with the scenario of quasi-static acceleration of electrons that generate a polar cap arc as they precipitate in the ionosphere. The detailed observations of the acceleration region by Cluster and the large scale image of the polar cap arc provided by TIMED are two different features of the same phenomenon. Combined together, they bring new light on the configuration of the high-latitude magnetosphere during prolonged periods of Northward IMF. Possible implications of the modelling results for optical observations of polar cap arcs are also discussed.

**Keywords.** Ionosphere (Polar ionosphere) – Magnetospheric physics (Magnetosphere-ionosphere interactions; Polar cap phenomena)

## 1 Introduction

During prolonged periods of northward IMF optical arcs are commonly observed above the polar cap ionosphere (e.g. Frank et al., 1982, 1986; Lassen and Danielsen, 1978; Burke et al., 1982; Carlson et al., 1988; Marklund et al., 1991). They consist of discrete and elongated optical structures generally oriented in the Sun-Earth direction (e.g. Valladares et al., 1994). Some of them extend across the entire polar cap, from the nightside to the dayside auroral regions (e.g. Frank et al., 1986). Such polar cap arcs are named “transpolar arcs” or “theta aurora” as they form a pattern looking like the

Greek letter “ $\theta$ ”. Other polar cap arcs have smaller scales. They are often referred to as “Sun-aligned arcs” and can be completely detached from the auroral oval or connected to it by only one end. Optical observations – from ground or spacecraft imagers – give interesting information about polar cap arcs geometry, motion and lifetime (see the review by Zhu et al., 1997). Polar cap arcs have relatively long lifetimes, they can last for more than one hour with only gradual variations of position and intensity (Hardy et al., 1982). They are elongated in the Sun–Earth direction and thin in the dawn–dusk direction. Several observations showed that polar cap arcs can drift at relatively low velocity in the dawn–dusk direction (e.g. Ismail et al., 1977; Hosokawa et al., 2011).

There is also clear evidence that they occur during quiet geomagnetic periods, with some delay after a northward turning of the IMF – estimated to about 1 h by Troshichev et al. (1988). However, about 20 % (Valladares et al., 1994) to 30 % (Rairden and Mende, 1989) of them are observed when the IMF  $B_Z$  is southward oriented suggesting that there is a delay between a southward turning of the IMF and the disappearance of polar cap arcs. Such a delay has been estimated from ground-based optical observations and it varies from 10–15 min (Troshichev et al., 1988) to 30 min (Valladares et al., 1994; Rodriguez et al., 1997). The influence of IMF  $B_Y$  and  $B_X$  on the PCA dynamics is even less understood. There is, however, some evidence that the polar cap arcs drift may be controlled by the IMF  $B_Y$  component, with a duskward/dawnward drift for positive/negative IMF  $B_Y$  (e.g. Ismail et al., 1977; Hosokawa et al., 2011).

In situ observations provide more detailed observations on the electrodynamics of polar cap arcs. Satellite data give unambiguous evidence that polar cap arc emissions are generated by precipitating electrons that have been accelerated along the magnetic field at magnetospheric altitudes. Many observations show that the precipitating electrons are accelerated by quasi-static field-aligned electric fields. Electron inverted-V spectra and potential drops above polar cap arcs were detected by rockets (Berg et al., 1994), by low altitude spacecraft like S3-2 (Burke et al., 1982), by Dynamic Explorer for a theta aurora (Frank et al., 1986) or Viking for transpolar arcs (Marklund et al., 1991). Both optical and in situ observations show that the field-aligned potential drop associated with polar cap arcs is relatively low, generally less than 2 keV (e.g. Hardy et al., 1982; Robinson and Mende, 1990; Huang et al., 1994). Furthermore, almost all observations associate polar cap arcs with upward field-aligned currents (Zhu et al., 1997).

Recently, the Cluster spacecraft provided observations of locally accelerated ion beams above the polar caps during periods of northward IMF. These so-called polar cap ion beams (PCIB) also show clear signatures of field-aligned acceleration by quasi-static electric fields (Maggiolo et al., 2006). A statistical analysis of 185 PCIB detected by Cluster between 2001 and 2006 revealed that PCIB have properties similar to the polar cap arcs (Maggiolo et al., 2011). PCIB are

elongated in the Sun–Earth direction, are associated with upward current sheets and have long lifetimes. PCIB dynamics shows similar dependency on IMF  $B_Z$  as PCA and they are associated with relatively weak field-aligned potential drops. Maggiolo et al. (2011) conjectured that PCIB correspond to a high altitude signature of the polar cap arcs.

Despite the numerous observations available, there is still a controversy about the magnetic topology, i.e. closed or open, of the polar cap arcs. Simultaneous observation of precipitating ions with typical plasmashet energies (e.g. Hoffman et al., 1985; Frank et al., 1986) suggests a closed field line geometry. However, other studies did not detect any ion precipitation (e.g. Whalen et al., 1971; Ismail et al., 1977). On the other hand, observation of relativistic electrons on magnetic field lines connected to polar cap arcs (Gussenhoven and Mullen, 1989) or observation of polar cap arcs embedded in the polar rain (e.g. Hardy et al., 1982) clearly favour the open field line geometry. The closed field line topology is often associated with large scale “theta aurora” while the open field line topology is preferentially associated with smaller scale polar cap arcs (e.g. Carlson et al., 2005). Several acceleration mechanisms and source regions have been proposed for polar cap arcs like the low-latitude boundary layer (LLBL), lobe reconnection tailward of the cusp or plasmashet extension in the lobe region (e.g. Bonnell et al., 1999, and references therein). Some polar cap arcs have also been associated with shear flow in the lobe region (e.g. Eriksson et al., 2006). A more recent study showed that the auroral arcs in the dayside auroral oval can expand poleward and fill the entire polar cap under a strong northward IMF lasting for hours (Zhang et al., 2009). However there is no consensus yet on the generator of polar cap arcs. It may be due to the existence of distinct types of polar cap arcs combined with the difficulty to link observations of polar cap arcs with in situ observations of the magnetosphere during prolonged periods of Northward IMF (e.g. Newell et al., 2009).

This study aims to combine in situ measurements by Cluster at the top of the acceleration region with optical observations from the TIMED spacecraft. We focus on observations taken on 1 April 2004. Around 06:24 UT, the TIMED spacecraft images the Northern polar cap and detects an isolated polar cap arc. Its width is of the order of tens of kilometres and it extends over more than 10 degrees of latitude in the North–South direction (see Fig. 1). About 20 min later the ion spectrometer onboard Cluster spacecraft detects an isolated inverted-V structure inside the lobe region on magnetic field lines mapping outside the field-of-view of the TIMED imager, but in the prolongation of the polar cap arc. The width and orientation of the inverted-V detected by Cluster is similar to the width and orientation polar cap arc imaged by TIMED.

In this paper, we propose a new method to compute the optical emission rates associated with the field-aligned acceleration structure probed by Cluster at high altitudes. The

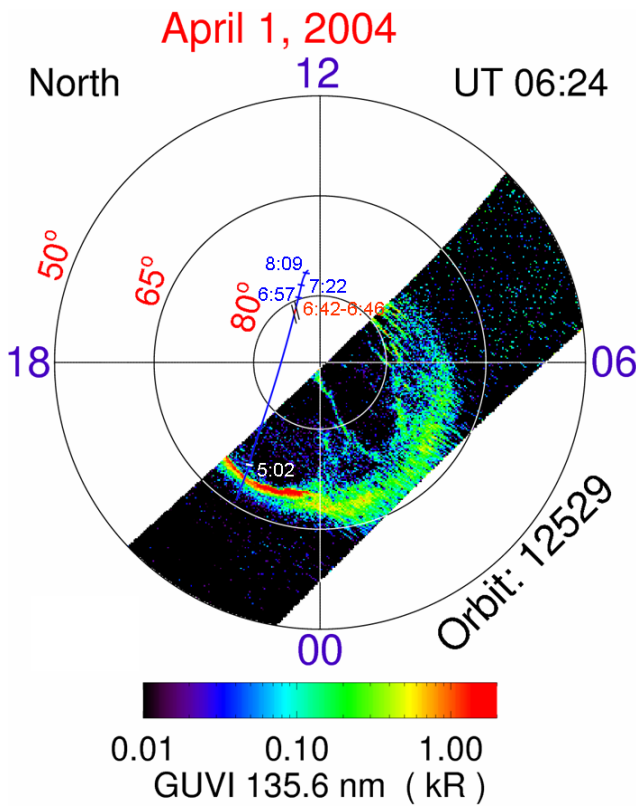


**Fig. 1.** GUVI image at a wavelength of 135.6 nm of the northern polar cap around 06:24 UT on 1 April 2004. The blue line shows the projection of Cluster 1 orbit above the northern polar cap from 04:40 to 08:25 UT. Cluster 1 orbit has been projected along magnetic field lines to an altitude of 200 km using the Tsyganenko 2004 model (Tsyganenko and Sitnov, 2005). The region where Cluster encounters the inverted-V structure is indicated in red.

method is based on three main modules: (i) Cluster data inside a PCIB, (ii) a kinetic magnetosphere-ionosphere (MI) coupling model providing the spectrum of precipitating electrons at ionospheric altitudes, given the input data specified by high-altitude Cluster observations; (iii) an ionospheric kinetic modelling package that provides the optical emission rates from the electron energy spectrum provided by the MI coupling model.

After a brief presentation of the methods and satellite data, we give a detailed description of Cluster and TIMED observations above the northern polar cap on 1 April 2004. We describe the MI and ionospheric modelling packages and explain how data from Cluster are integrated in these models. Finally, we compare the modelled optical emission rates for the OI (135.6 nm) line with the observations by TIMED in the same wavelength band. In the last section, we discuss the possible application of this method for the combined analysis of optical and in situ data. We also examine the magnetospheric configuration during this event to portray the broader geophysical context of our analysis.

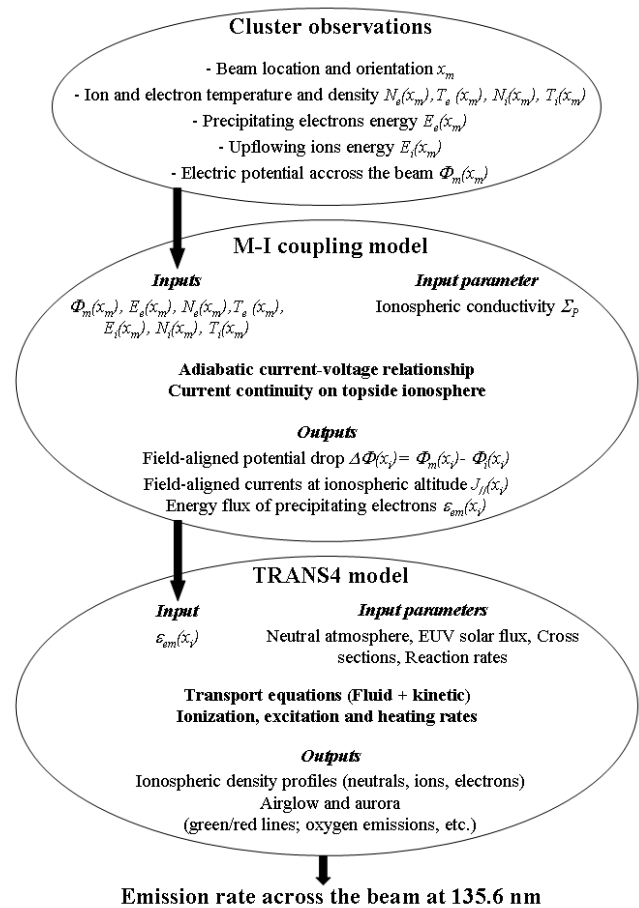


**Fig. 2.** Block diagram summarizing the data and models used in this study. The inputs and outputs of each block are indicated.

## 2 Instrumentation and method

The four identical Cluster satellites have been launched in 2001 on an elliptical orbit ( $4.0 \times 19.6 R_E$ ) with an inclination of  $90^\circ$ . A detailed description of the Cluster mission can be found in Escoubet et al. (2001). Ion velocity distribution functions and their moments, ion energy spectrograms and pitch angle distributions for ions with energies between  $\sim 0$  and  $40 \text{ keV } q^{-1}$  are provided by the Cluster Ion Spectrometers (CIS) onboard the Cluster spacecraft 1, 3 and 4 (Rème et al., 2001). CIS consists of two different ion spectrometers, the Composition and Distribution Function analyzer (CODIF), which can resolve the major magnetospheric ions and the Hot Ion Analyzer (HIA) which is not mass discriminating but has higher angular and energy resolutions. Electron data are provided by the PEACE experiment which detects the electron fluxes between 0 and 26 keV (Johnstone et al., 1997). In addition, we use electric field data from the Electron Drift Instrument (EDI) (Paschmann et al., 2001). Magnetic field data are provided by the Cluster Fluxgate Magnetometers (FGM) (Balogh et al., 2001).

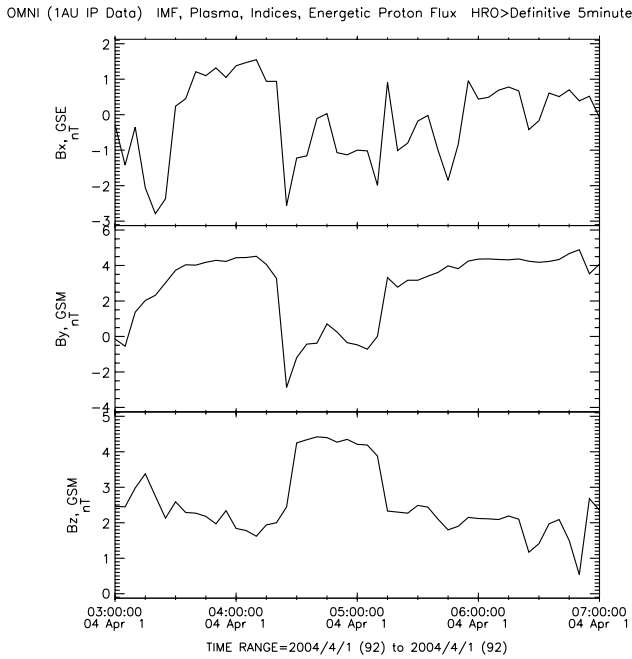


**Fig. 3.** IMF components in the GSM frame from the ACE spacecraft on 1 April 2004 from 03:00 UT to 07:00 UT. Data have been shifted to 1 AU. The time shift is computed at the bow shock and provided by the OMNI database.

We also use density measurement from the WHISPER experiment (Décréau et al., 2001). The plasma density can be estimated without bias by WHISPER from the analysis of characteristic plasma frequencies in wave spectrograms.

The Global Ultraviolet Imager (GUVI) is one of the four scientific instruments on board the NASA's Thermosphere Ionosphere Mesosphere Energetics and Dynamics (TIMED) satellite (see Christensen et al., 2003). TIMED was launched on 7 December 2001 into a 630 km circular polar orbit with an inclination of  $74^\circ$ . GUVI provides cross-track scanned images of the Earth's ultraviolet airglow and aurora emission in the far ultraviolet (FUV) in five selectable wavelength channels from 115.0 to 180.0 nm wavelength. Major emission features include H I (Lyman  $\alpha$ , 121.6 nm), OI (130.4 nm), OI (135.6 nm) lines, N<sub>2</sub> Lyman-Birge-Hopfield short bands (LBHS, 140.0–150.0 nm), and N<sub>2</sub> Lyman-Birge-Hopfield long bands (LBHL, 165.0–180.0 nm). The sensitivity of the GUVI instrument at 135.6 nm is approximately  $0.5 \text{ counts s}^{-1} \text{ Rayleigh}^{-1} \text{ pixel}^{-1}$  (Humm et al., 1998), with a typical spectral resolution of 0.4 nm (Christensen et al., 2003). The images are generated using a microprocessor-controlled cross-track scan mirror mechanism that scans the disk beginning  $60^\circ$  from nadir on the sunward side across the disk and through the limb on the anti-sunward side of the satellite (Paxton et al., 1999). The TIMED/GUVI data provide opportunities for identifying auroral structures and features, such as auroral arcs in the oval and the polar cap

(Zhang et al., 2005a, b, 2006, 2009), ring current aurora (Zhang et al., 2008) and a new empirical global auroral model (Zhang and Paxton, 2008).

Data from Cluster, the electric potential from integrated electric field,  $\Phi_m(x_m)$ , the ion and electron density and temperature  $N_i(x_m)$ ,  $N_e(x_m)$ ,  $T_i(x_m)$ ,  $T_e(x_m)$ , the magnetic field  $B_m(x_m)$ , are introduced as the magnetospheric boundary condition of the magnetosphere-ionosphere coupling model (Echim et al., 2007, 2008). The MI coupling model is described in detail in Sect. 4.1. It provides the electric potential at ionospheric altitudes,  $\Phi_i(x_i)$ , and the field-aligned potential drop  $\Phi_m(x_i) - \Phi_i(x_i)$ , as a function of the distance across the arc,  $x_i$ . It also provides the energy spectrum of the precipitating electrons that is an input for the kinetic modelling of the ionospheric aurora and airglow. The kinetic model for the electron transport in the ionosphere (TRANS4) is described in detail in Sect. 4.2. This model computes the steady-state ionospheric profiles. It uses an input the spectrum of precipitating electrons provided by the MI coupling model and computes the resulting optical and UV emissions as a function of the distance across the structure. The TRANS4 emission rates can then be compared with TIMED-GUVI observations. A diagram of the coupling between the models and data is given in Fig. 2.

### 3 Observations

On 1 April 2004, between 05:00 UT to 07:00 UT the Cluster spacecraft are located above the northern polar ionosphere in the region mapping to the magnetospheric lobes. During this time interval the TIMED spacecraft orbits above the Northern Hemisphere and images the high latitude ionosphere from  $\sim 06:04$  UT to  $\sim 06:44$  UT. In this section we give a detailed description of Cluster and TIMED data during this time period.

#### 3.1 Interplanetary and geomagnetic conditions

Figure 3 shows the components of the interplanetary magnetic field measured by the ACE spacecraft on 1 April 2004 from 03:00 UT to 07:00 UT and shifted to 1 AU. During this period the IMF is relatively steady; a weak negative  $B_X$  ( $\sim -0.5$  nT), and positive  $B_Y$  ( $\sim 4$  nT) and a Northward  $B_Z$  ( $\sim 2.5$  nT).  $B_Z$  remains positive for the entire time interval while  $B_X$  and  $B_Y$  change sign. Indeed, despite these relatively steady conditions, we can distinguish three IMF regimes: (A) from 03:30 UT to 04:30 UT all components are positive ( $B_X \sim 1$  nT,  $B_Y \sim 4$  nT and  $B_Z \sim 2$  nT), (B) between 04:30 UT to  $\sim 05:30$  UT  $B_X$  turns negative ( $\sim -1$  nT),  $B_Y$  is almost null and  $B_Z$  is strongly positive ( $\sim 4$  nT), (C) from 05:30 UT to 07:00 UT the IMF conditions are stable and similar to what was observed before 03:30 UT. SuperDARN data for this time period (not shown) reveal that the convection pattern is somewhere in-between the four-cell convection

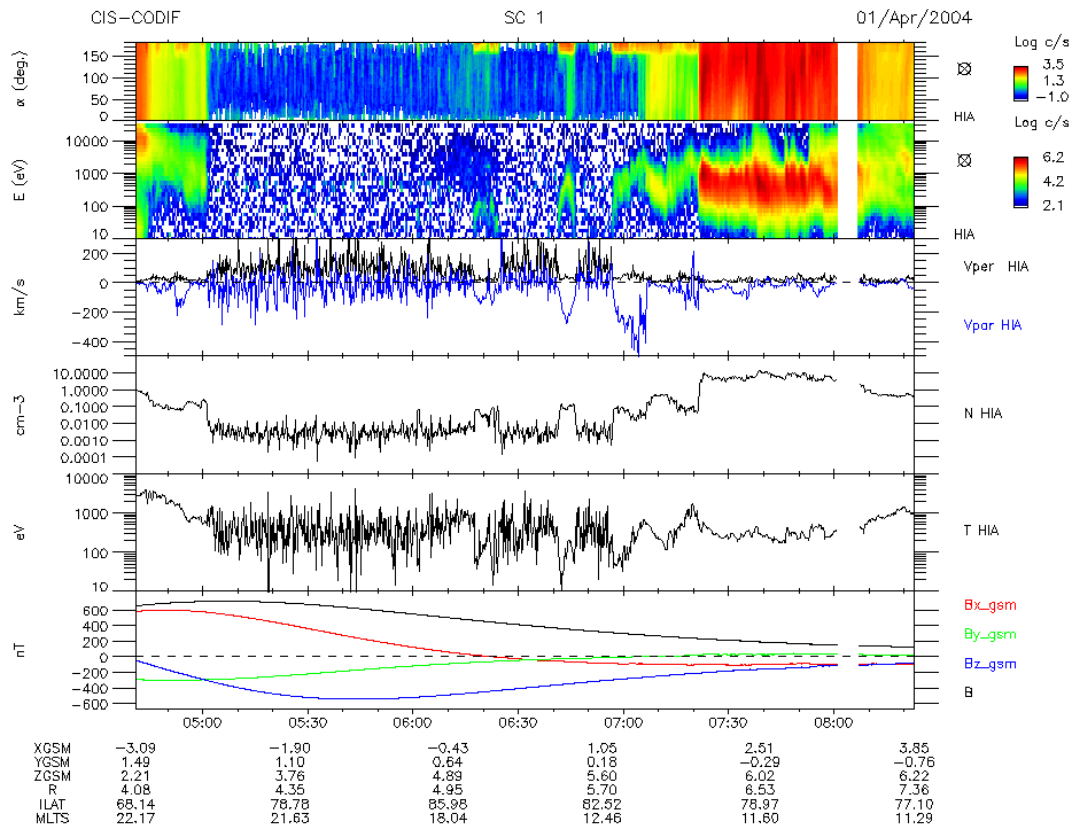


**Fig. 4.** Data from Cluster 1 on 1 April 2004 from 04:40 UT to 08:25 UT. From top to bottom: ion pitch angle distribution from HIA for all ions; time-energy spectrogram from HIA for all ions; ion velocity perpendicular (black) and parallel (blue) to the magnetic field from HIA; ion density from HIA; ion temperature from HIA, GSE components and magnitude of the magnetic field from the FGM experiment. The regions where the ion velocity, density and temperature are highly fluctuating correspond to the magnetospheric lobes where the plasma is too cold to be measured by the HIA experiment. These fluctuations are mainly due to instrumental noise.

pattern, which is believed to be driven by lobe reconnection during periods when IMF  $B_Z$  is dominating, and the distorted two-cell pattern typical for periods when IMF  $B_Y$  is dominating and drives asymmetrical dayside reconnection (e.g. Haaland et al., 2007).

The low geomagnetic activity expected for such a long period of northward IMF is confirmed by the low values of the  $K_p$  index ( $K_p=0^+$  from 03:00–06:00 UT and  $K_p=1$  from 06:00–09:00 UT) and the low values of the DST index that takes a minimum value of  $-12$  nT between 03:00 UT and 07:00 UT. A weakly active period, the only one during this time interval, is signaled by a slight increase of the AE index from about 50 nT at 06:40 UT to 110 nT at 07:00 UT.

### 3.2 Cluster observations

This study focuses on the analysis of an inverted-V structure observed above the northern polar cap. This event, referred to as a polar cap ion beam (PCIB), is extracted from a set of 185 events studied by Maggiolo et al. (2011).

Figure 4 shows data from Cluster 1 on 1 April 2004 from 04:40 UT to 08:20 UT. During this time period the spacecraft

orbits from the nightside magnetosphere to the dayside magnetosphere in the Northern Hemisphere. The ionospheric projection of the spacecraft orbit during this time period can be found in Fig. 1.

Before 05:02 UT Cluster 1 is located in the nightside plasmasheet and crosses magnetic field lines mapping to the auroral zone. It detects an isotropic plasma population with typical plasmasheet density and temperature ( $N \sim 0.1$ – $0.2$   $\text{cm}^{-3}$ ,  $T \sim 1$ – $2$  keV). From 05:02 UT to 06:57 UT Cluster 1 is located in the magnetospheric lobes above the northern polar cap. The magnetospheric lobes are filled with cold plasma which is not energetic enough to overcome the spacecraft positive potential and enter the particle detectors (e.g. Engwall et al., 2009; Yau et al., 2007). They are, thus, clearly identified in HIA data as a region where no plasma is measured and, thus, where the density is very low. Consequently the density, velocity and temperature provided by HIA in this region are not reliable and are highly fluctuating due to the instrumental noise. From 06:06 UT to 06:25 UT a tenuous cloud of isotropic plasma ( $N < 0.01$   $\text{cm}^{-3}$ ,  $T \sim 1$  keV) is detected (see first two panels of Fig. 4). At its poleward

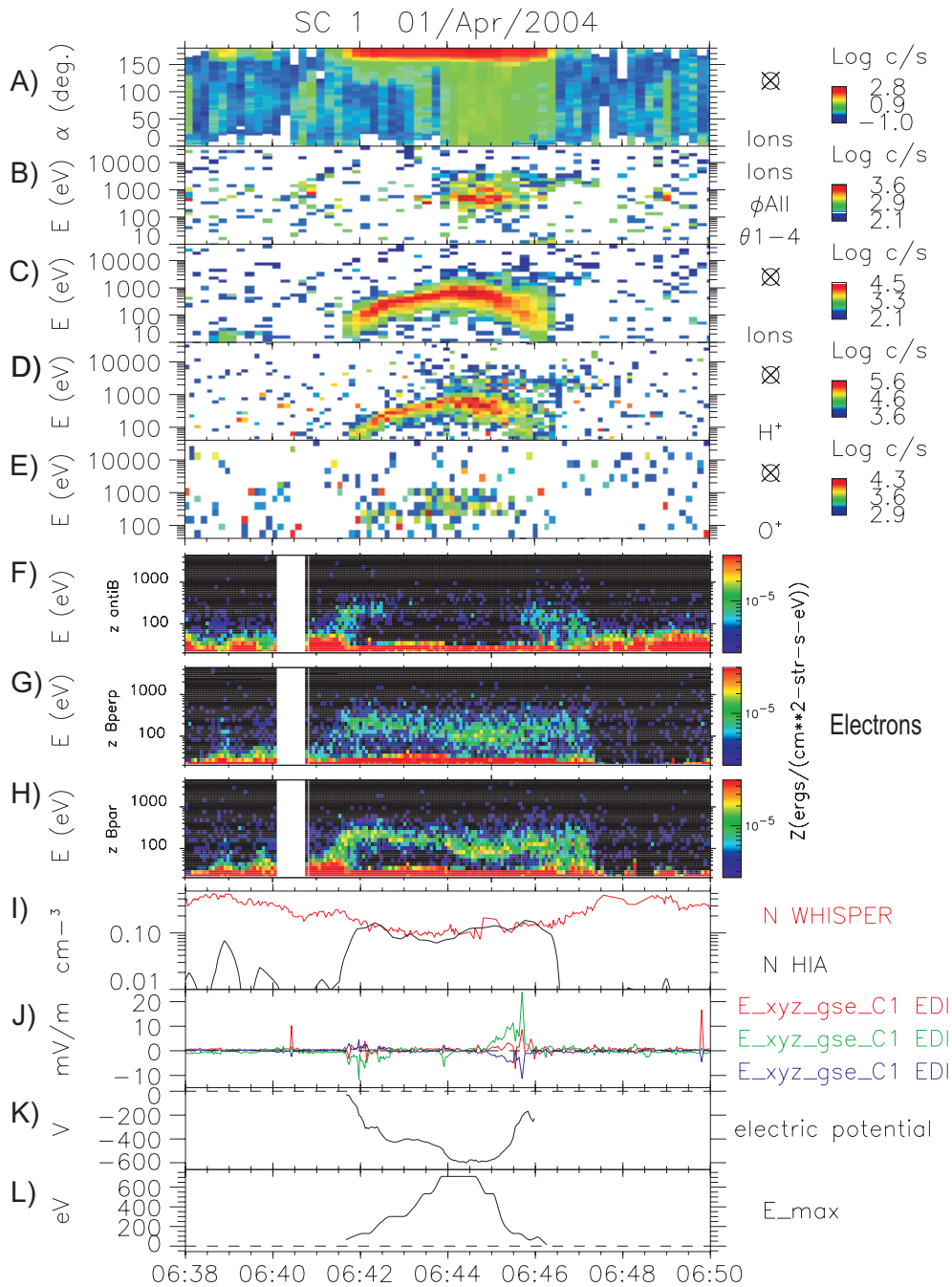


**Fig. 5.** Data from Cluster 1 on 1 April 2004 from 06:38 UT to 06:50 UT. From top to bottom: **(a)** ion pitch angle distribution from HIA for all ions; **(b)** time-energy spectrogram from HIA for ions with pitch angles between 0° and 150°; **(c)** time-energy spectrogram from HIA for all ions; **(d)** time-energy spectrogram from CODIF for H<sup>+</sup>; **(e)** time-energy spectrogram from CODIF for O<sup>+</sup>; **(f)** time-energy spectrogram for upgoing electrons; **(g)** time-energy spectrogram for electrons perpendicular to the magnetic field; **(h)** time-energy spectrogram for downgoing electrons; **(i)** ion density from HIA (black) and ion density from WHISPER (red); **(j)** electric field components in the GSE frame from EDI; **(k)** electric potential along the spacecraft trajectory computed from the EDI electric field; **(l)** Energy of maximum of flux from HIA.

side, two weak upflowing ion beams are measured. They consist of cold plasma strongly field-aligned and presumably of ionospheric origin. These beams have a low energy (~100 eV) and Cluster crosses them in about 1 min which

implies that they are very thin (less than ~15 km at ionospheric altitude).

The PCIB of interest for this study is detected by Cluster 1 between 06:41:30 and 06:46:30 UT. This upgoing ion

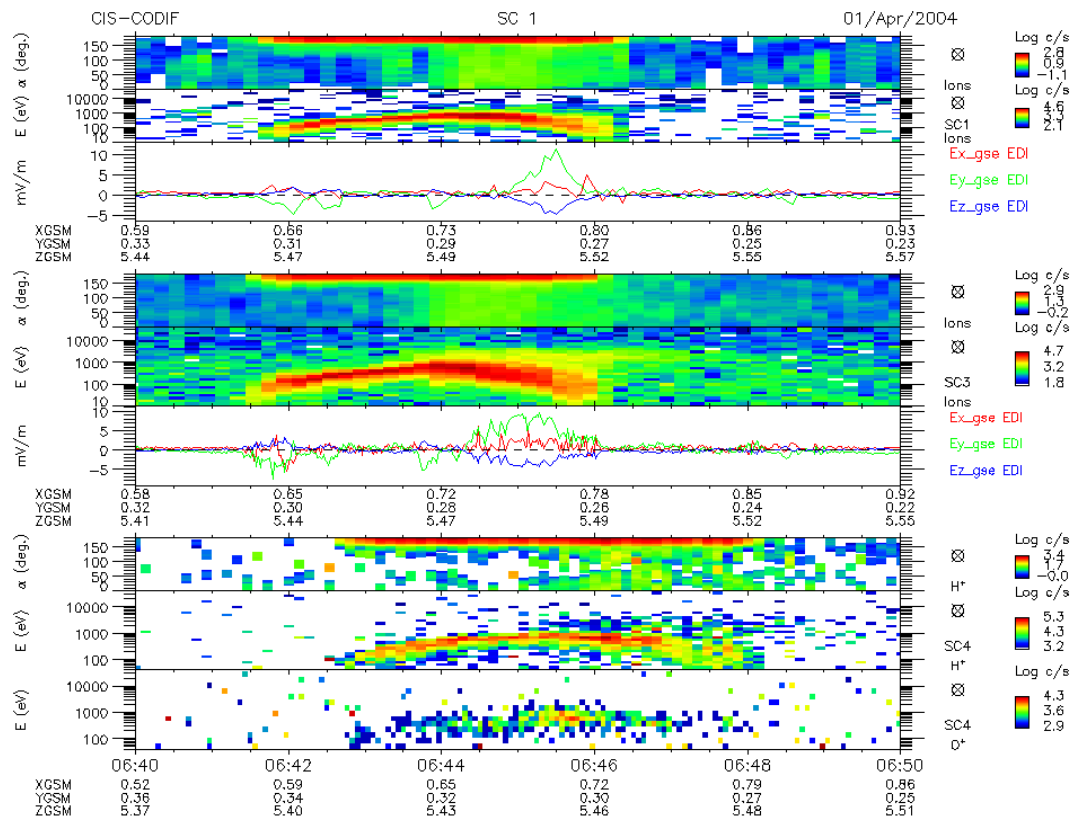


**Fig. 6.** Data from the Cluster spacecraft on 1 April 2004 from 06:40 UT to 06:50 UT. From top to bottom: Pitch angle spectrogram from HIA for all ions, spacecraft 1; time-energy spectrogram from HIA for all ions, spacecraft 1; GSE components the electric field from the EDI experiment, spacecraft 1; spacecraft 1 position in earth radii in the GSM frame; pitch angle spectrogram from HIA for all ions, spacecraft 3; time-energy spectrogram from HIA for all ions, spacecraft 3; GSE components the electric field from the EDI experiment, spacecraft 3; spacecraft 3 position in Earth radii in the GSM frame; pitch angle spectrogram from HIA for protons, spacecraft 4; time-energy spectrogram from CODIF for O<sup>+</sup>, spacecraft 4; time-energy spectrogram from CODIF for protons, spacecraft 4; spacecraft 4 position in Earth radii in the GSM frame.

beam displays a nice inverted-V structure and the ion energy reaches 700 eV in its centre, as shown by the energy distribution in Fig. 4. This structure will be discussed in more detail below. After 06:57 UT the spacecraft exits the lobe region and enters the dayside auroral zone, a relatively large acceleration region where it detects field-aligned upflowing ionospheric ion beams with energies up to 2.5 keV. They are accompanied by an isotropic population after 07:05 UT. This region is adjacent to the poleward side of the cusp where Cluster enters around 07:22 UT and exits at 08:09 UT.

Figure 5 shows an enlarged view of the inverted-V structure detected from 06:41:30 UT to 06:46:30 UT by Cluster 1. As shown by the ion pitch angle distribution in panel (a), it consists of strongly field-aligned upflowing ions (180° pitch angle in the Northern Hemisphere corresponds to upward flow). The pitch angle distribution evidences the presence of another ion population, isotropic, in the right (poleward) side of the inverted-V between 06:44 UT and 06:46:30 UT. Panel (b) of Fig. 5 shows a time-energy spectrogram from HIA for selected angular sectors removing ions

with pitch angles comprised between 150° and 180°. It excludes upflowing ions and evidences this isotropic population which has a temperature of about 500 eV and a low density ( $\sim 0.002 \text{ cm}^{-3}$ ). Such association between PCIB and isotropic ions is very common. About 40% of PCIB are accompanied by isotropic ions. The temperature and pitch angle distribution of this isotropic component suggest that it may originate from the Cold Dense Plasma Sheet. However, the processes that bring it into the magnetospheric lobes are still not understood (Maggiolo et al., 2011). It is very unlikely that the source of this population is the upflowing ions. Indeed, upflowing ions contain a significant proportion of O<sup>+</sup> ions while the isotropic component only consists of H<sup>+</sup>. Furthermore, they are only detected in the poleward side of the PCIB and have energy slightly higher than the upflowing ions (see Fig. 5d).

In the centre of the PCIB the H<sup>+</sup> and O<sup>+</sup> density measured by CODIF are respectively of  $\sim 0.1 \text{ cm}^{-3}$  and  $\sim 0.01 \text{ cm}^{-3}$ . The density inside the PCIB is, thus, dominated by the upflowing H<sup>+</sup> ions ( $\sim 90\%$ ) with a small amount of upflowing

$O^+$  ions ( $\sim 10\%$ ) while the contribution of the isotropic ions to the total density is almost negligible. A statistical analysis of the upflowing ion composition and of the density of the isotropic population inside PCIB can be found in Maggiolo et al. (2011).

Together with their low temperature ( $\sim 150$  eV) and their pitch angle distribution, the presence of  $O^+$  ions confirms the ionospheric origin of the upflowing ions. Because of the low flux of  $O^+$ , it is difficult to estimate precisely the oxygen ions energy using Cluster 1 data (Fig. 5). However, it can be done with Cluster 4 CODIF data which show that both  $O^+$  and  $H^+$  have the same energy profile across the structure (Fig. 6).

Inside the inverted-V structure the density measured by the HIA ion detector and the density computed from WHISPER wave data are in good agreement, as shown by panel (i) of Fig. 5, indicating that the plasma is accurately measured by HIA in this region. However, outside the inverted-V, HIA and WHISPER densities differ significantly. While WHISPER detects plasma inside and outside the beam, HIA detects no ions outside the inverted-V region. This discrepancy is not surprising as lobe ions are too cold to be measured by HIA. However, the lobe plasma can be measured indirectly by probing the plasma frequency with WHISPER. Thus, the comparison between WHISPER and HIA densities gives unambiguous evidence that the inverted-V is surrounded by cold lobe plasma. Furthermore, contrary to what is suggested by particle spectrograms, the density in the outflow region ( $\sim 0.1$  cm $^{-3}$ ) is lower than the density in the lobe region ( $0.2$ – $0.4$  cm $^{-3}$ ). Using these densities we can estimate the flux of outflowing particles. In the centre of the PCIB, the particle field-aligned velocity is of about  $250$  km s $^{-1}$  and the particle flux of  $\sim 2.5 \times 10^7$  cm $^{-2}$  s $^{-1}$  at Cluster altitude. Outside the PCIB, the cold ions field-aligned velocity must be lower than  $70$  km s $^{-1}$  otherwise it would be detected by the CIS experiments. Using this velocity and a density of  $0.4$  cm $^{-3}$  in the lobe region, we obtain an upper estimate of the particle flux in the lobe similar to the flux inside the PCIB. According to estimates made with the EFW experiment onboard Cluster in the same region, the average upward velocity of cold ions in the lobe is  $32$  km s $^{-1}$  (Engwall et al., 2009). In that case the flux in the lobes may be slightly lower, of the order of  $1.3 \times 10^7$  cm $^{-2}$  s $^{-1}$ . That particle fluxes inside and outside the PCIB are similar reveals that for this particular event ionospheric processes may not be required to account for the observed flux of particles inside PCIB.

The density in the lobe regions is comparable on the two sides of the PCIB. Similarly on both sides of the PCIB the electric field is comparable. It is weak ( $\sim 1$  mV m $^{-1}$ ), mainly directed in the downward direction with a weak positive component along the  $X_{GSE}$  (the average electric field in the GSE frame is  $[0.3, -0.7, 0.1]$  mV m $^{-1}$ ). The convection around the PCIB is, thus, directed in the sunward direction with a low convection velocity of  $\sim 3$  km s $^{-1}$  at Cluster altitude ( $\sim 0.3$  km s $^{-1}$  at ionospheric altitude).

The convection electric field inside the PCIB is difficult to estimate as the electric field is dominated by a strong convergent electric field associated with the upflowing ion beam (panel f of Fig. 5). This perpendicular electric field reaches values comprised between  $10$ – $20$  mV m $^{-1}$ , well above the surrounding convection electric field level. Such large convergent electric fields located at the edges of the inverted-V are consistent with a U-shaped potential profile associated with the presence of parallel electric fields at lower altitudes, (e.g. Mozer et al., 1977; Johansson et al., 2006). The electric potential along Cluster trajectory computed from EDI electric field data is plotted in panel (g). Assuming a reference value of the electric potential,  $\Phi_m = 0$ , at the left edge of the inverted V, we obtain a potential drop,  $\Delta_{\perp} \Phi$ , of about  $700$  V across the structure. Such profile is similar to the electric potential profile advocated by quasi-stationary models of stable discrete auroral arcs (Lyons, 1980; Echim et al., 2007; de Keyser et al., 2010). These models demonstrate that  $\Delta_{\perp} \Phi$ , the perpendicular potential drop corresponding to a perpendicular convergent electric field, sustains a field-aligned potential drop  $\Delta_{\parallel} \Phi$  at lower altitudes. It has also been shown (e.g. Vaivads et al., 2003) that the maximum of  $\Delta_{\perp} \Phi$  is of the order of the maximum of  $\Delta_{\parallel} \Phi$ . The maximum of  $\Delta_{\perp} \Phi$  (and of  $\Delta_{\parallel} \Phi$  as discussed above) is in agreement with the energy of maximum of flux the upflowing ions (panel h) measured by Cluster. That the upflowing  $O^+$  and  $H^+$  have similar energy profiles which correspond to the electric potential variation across the PCIB indicates that the ion upward acceleration is caused by a quasi-static electric field parallel to the magnetic field and located below the Cluster spacecraft. Panels (f), (g) and (h) of Fig. 5 show PEACE data, respectively, for upgoing, perpendicular and downgoing electrons. The electrons temperature is of the order of  $120$  eV. Almost no electrons are detected in the upward direction. In the perpendicular and downward directions the electron energy peaks between  $80$  eV and  $150$  eV except on the left edge of the inverted-V where it peaks around  $200$  eV. Such electron signature is typical for PCIB. It evidences a downward acceleration of electrons which is interpreted as a signature of a field-aligned potential drop located above the spacecraft (e.g. Maggiolo et al., 2006). Cluster is, thus, crossing the field-aligned acceleration region. Except for the left edge of the inverted-V, most of the acceleration occurs below Cluster and according to the ion and electron peak energy, less than  $25\%$  of the total field-aligned potential drop is located above Cluster altitude.

The orientation of the structure can be obtained by a minimum variance analysis (MVA) of electric field data. We assume that the outflow region can be described as a planar structure parallel to the magnetic field lines surrounded by strong convergent electric fields perpendicular to the beam plane and to the magnetic field. The axis of maximum variance corresponds to the direction of this strong convergent electric field. The associated PCIB direction is then given by the cross product between the maximum variance axis and

the magnetic field direction. The MVA analysis assumes that the quasi-static bipolar electric field dominates the electric field measured by the Cluster spacecraft and that temporal variations can be neglected. This assumption is justified by the stationarity of PCIB (Maggiolo et al., 2011, see also below for this particular event) and by the large amplitude of the bipolar electric field compared to any other electric field fluctuations observed during this event.

For an accurate estimation of the MVA frame, the eigenvalues of the electric variance matrix must fulfill satisfactorily the condition  $\lambda_1 \gg \lambda_2 \gg \lambda_3$  where  $\lambda_1$ ,  $\lambda_2$  and  $\lambda_3$  are, respectively, the maximum, intermediate and minimum variances. The three components of the electric field are computed from EDI under the hypothesis that there is no electric field along the magnetic field. Thus, the minimum variance axis is always oriented along the magnetic field and  $\lambda_3$  is always almost null and  $\ll \lambda_1, \lambda_2$ . Moreover, it implies that the intermediate variance axis gives the PCIB direction.

We apply this method to the electric field measured by Cluster 1 EDI from 06:41:30 to 06:46:30; i.e. from the beginning to the end of the bipolar electric field signature. The ratio between the maximum and intermediate variance is 8.32 showing that the MVA frame is relatively well defined. The intermediate variance axis ( $[-0.9615; -0.232; 0.1219]$  in the GSE frame), shows that the outflow region extends approximately in the Sun-Earth direction as expected for PCIB (Maggiolo et al., 2011). We obtain a similar orientation for the MVA frame when applying the MVA analysis to each side of the PCIB separately as the electric field on one side of the PCIB is almost antiparallel to the electric field on the other side of the PCIB.

Figure 6 displays data from the three Cluster spacecraft on which the CIS experiment is operating from 06:40 UT to 06:50 UT. During this time interval, the spacecraft separation is relatively small. Cluster 1 and 3 are separated by 200 km while Cluster 4 is located about 600 km behind them. The inverted-V structure is clearly identified in the particle spectrograms from these three spacecraft. Cluster 1 and 3 detect it roughly at the same time (respectively, from 06:41:37 UT to 06:46:16 UT and from 06:41:27 UT to 06:46:03 UT) and Cluster 4 about 2 min after (from 06:42:52 UT to 06:48:06 UT). Note that these crossing times are obtained by a visual inspection of particle spectrograms and consequently suffer from uncertainty.

The orbits of the three Cluster spacecraft in the  $(XY)_{\text{GSM}}$  plane for this time period are plotted in Fig. 7. The magnetic field is mainly directed along the  $Z_{\text{GSM}}$  direction so that the  $(XY)_{\text{GSM}}$  plane roughly corresponds to the plane perpendicular to the magnetic field. The orientation of the PCIB deduced from the minimum variance analysis is indicated on the figure as well as the location of the spacecraft when they enter/exit the ion inverted-V. The location of the ion inverted-V event from Cluster 1 and 3, which cross it at approximately the same time, is in good agreement with the orientation of the convergent electric field structure obtained from EDI data

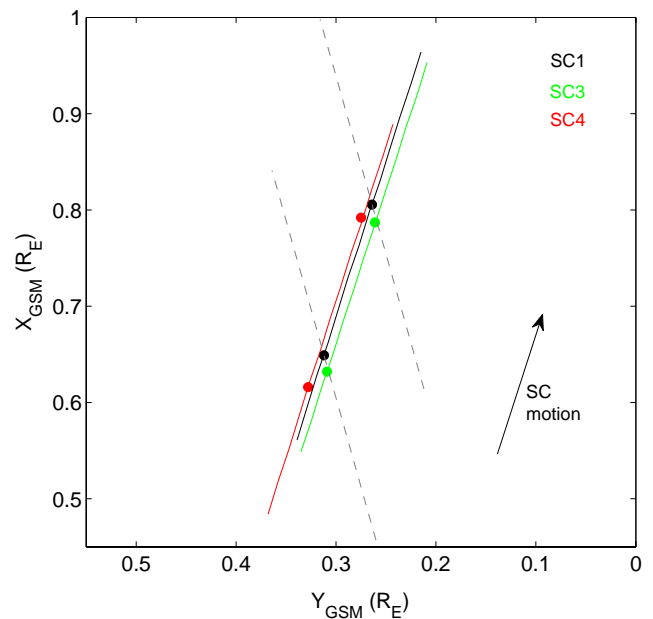


**Fig. 7.** Cluster 1 (black), Cluster 3 (green) and Cluster 4 (red) orbits in the XY GSM plane from 06:40 UT to 06:50 UT on 1 April 2004. The coloured disks represent the boundaries of the PCIB as identified by a visual inspection of particle spectrograms. The grey-dotted lines represent the PCIB orientation as deduced from a minimum variance analysis of Cluster 1 electric field.

by minimum variance analysis. Cluster 4 detects the ion inverted-V later and slightly shifted in the  $+Y_{\text{GSM}}$  direction, possibly an effect due to the drift of the arc. In that case the drift velocity would be low, comprised between  $0.42 \text{ km s}^{-1}$  and  $1.23 \text{ km s}^{-1}$  at Cluster altitude (i.e. between  $\sim 40 \text{ m s}^{-1}$  and  $120 \text{ m s}^{-1}$  at a typical ionospheric altitude of 100 km) depending on whether we choose, as a reference, the equatorward or poleward side of the PCIB. Note that the motion of the PCIB during this event is in agreement with polar cap arc drift. Several studies reported polar cap arc drift velocities in the range of a few hundred  $\text{m s}^{-1}$  or less (e.g. Ismail et al., 1977; Hosokawa et al., 2011). Furthermore, the PCIB moves in the direction of the IMF  $B_Y$  component. This is consistent with the observations of Valladares et al. (1994) and Hosokawa et al. (2011) that stable polar cap arcs drift in the IMF  $B_Y$  direction.

### 3.3 TIMED observations

On the same day and during the same time period, the TIMED spacecraft crosses the northern polar cap region in the postmidnight-afternoon direction. The GUVI imager onboard TIMED images the northern ionosphere from 06:04 UT to 06:44 UT.

The GUVI image of the OI emission line at 135.6 nm (Fig. 1) reveals the presence of an isolated polar cap arc. The arc is elongated in the postnoon-premidnight direction and is inclined by  $20^\circ$  with respect to the Sun-Earth direction. It

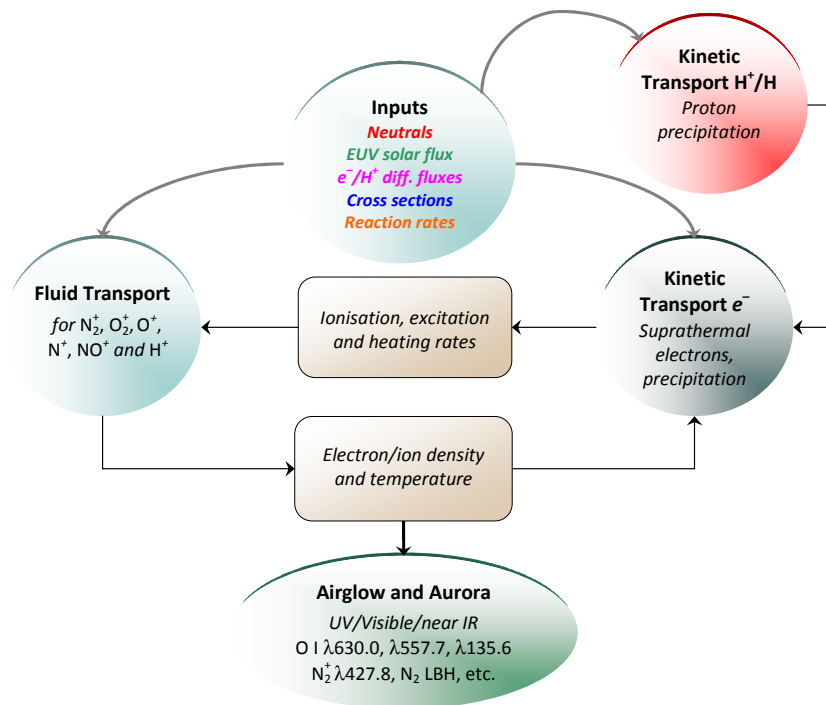


**Fig. 8.** Synopsis of the electron/proton/hydrogen kinetic/fluid model TRANS4 (see for instance Simon et al., 2007).

is almost perpendicular to the TIMED orbit and, therefore, is spatially thin along the orbit. As the GUVI imager scans line by line perpendicularly to TIMED trajectory, it implies that the arc has been measured in a very short time period. The detection time is 06:23 in the centre of the image (i.e. about 20 min before the Cluster spacecraft detect the PCIB) and 06:23:40 at the left edge of the image. Consequently, no significant distortion due to a possible drift of the arc while GUVI was scanning the polar cap is expected. Thus, the actual shape and width of the arcs should be well represented on the image.

The polar cap arc detected by TIMED-GUVI is connected to the midnight oval and bends toward the morning sector. This is a characteristic feature of the “hook-shaped” class of polar cap arcs (Murphree et al., 1982; Ismail and Meng, 1982). The arc crosses the whole GUVI field of view and, thus, could possibly connect to the dayside auroral zone and form a theta aurora across the entire polar cap as previously reported for “hook-shaped” arcs by Frank et al. (1982).

The poleward part of the arc, at the left side of the image is affected by edge and look angle effect which makes it appearing brighter and thicker. Actually the width and intensity of the arc are fairly constant all along it. Their best estimation is obtained in the centre of the image where GUVI observes at nadir. The nadir intensity at 135.6 nm is around 230 R and the width at half maximum intensity is 37 km.

On the GUVI image the auroral oval is identified as a circular region of intense emission. Its poleward boundary is

located at an invariant latitude of about  $72^\circ$  in the nightside and of about  $80^\circ$  in the afternoon region. The polar cap, i.e. the region of the ionosphere connected to the magnetospheric lobes, is identified as dark region located at higher latitude than the auroral oval. Some diffuse emission in the nightside at latitudes higher than the auroral oval can be noticed in a region delimited by the noon-midnight meridian and the polar cap arc. However, at latitudes higher than  $80^\circ$ , the arc is clearly isolated in the middle of the polar cap.

The projection of the Cluster 1 orbit is superposed to the GUVI image (Fig. 1). Cluster location and the corresponding times at the transitions between the main regions identified with HIA are also indicated. There is a good agreement between Cluster observations and the TIMED image. The plasmashet-lobe boundary detected by Cluster at 05:02 UT is approximately collocated with the poleward boundary of the auroral oval evidenced by the TIMED-GUVI image. Similarly, Cluster enters the dayside auroral zone at 06:57 UT at an invariant latitude of  $80^\circ$  comparable to the latitude of the poleward boundary of the prenoon auroral oval obtained from the GUVI image.

PCIB are associated with field-aligned electric fields that accelerate electrons downwards. These precipitating electrons may trigger photo-emissions as they collide with ionospheric particles. Thus, in principle, the PCIB may produce optical emissions that can be detected by the GUVI imager. Furthermore, an association between PCIB and polar cap arcs has already been suggested because of the similarities

between PCIB and polar cap arcs statistical properties (Maggiolo et al., 2011). For this particular event, there are indeed several similarities between Cluster and TIMED observations. Red indicates the footprint of the field lines where Cluster 1 detects the PCIB. The two parallel black solid lines correspond to a projection of the PCIB according to its size and orientation as estimated with Cluster data. It has a similar geometry (i.e. similar size and orientation) as the polar cap arc imaged by TIMED. In addition, the PCIB is located in the prolongation of the arc and both are isolated structures in the lobe/polar cap region.

These similarities suggest that both spacecraft may observe the same structure, TIMED imaging its low-altitude part and Cluster sampling the acceleration region at higher altitudes. However, it is difficult to have an unambiguous proof of this correlation. Indeed, Cluster is outside the GUVI field-of-view and about 20 min separate Cluster and TIMED observations. Consequently, the polar cap arc measured by TIMED may not extend up to Cluster location in the day-side polar ionosphere. It is also possible that the PCIB measured by Cluster is associated with a polar cap arc but distinct from the one imaged by TIMED. Furthermore, both structures may have moved, evolved or disappeared during the 20 min separating both observations. However, this delay between observations must be considered, taking into account the stability of PCIB and polar cap arcs. Both have been shown to have long lifetimes and may stay stable for long time periods; more than 20 min for PCIB (Maggiolo et al., 2011) and up to more than one hour for polar cap arcs (see, for instance, Zhu et al., 1997, or Kullen and Janhunen, 2004). During this event, the IMF is stable, so that such long lifetime and stationarity can be expected. This seems to be confirmed by Cluster data that show no significant evolution of the PCIB during the two minutes of the pass. Furthermore, the PCIB drift velocity is low and would correspond to a displacement of a maximum of  $1.5^\circ$  in 20 min.

To further investigate the link between both structures, an estimation of the photo-emissions triggered by the PCIB is required. It will be done using models to compute the emissions at 135.6 nm produced by precipitating electrons accelerated downwards through the field-aligned potential drop observed by Cluster.

#### 4 Modelling

The UV emission observed by TIMED-GUVI and the fluxes of precipitating electrons collocated with the PCIB have been modelled by a combination of electrostatic modelling of the magnetosphere-ionosphere coupling (Echim et al., 2007, 2008) and a kinetic-fluid model (TRANS4) for auroral emissions (Lilensten and Blelly, 2002; Simon et al., 2007). In this section, we discuss in detail the two numerical models used to simulate the photo-emission at 135.6 nm triggered by the PCIB observed by Cluster.

#### 4.1 Magnetosphere-ionosphere coupling model

Convergent magnetospheric electric fields play the role of generators of the auroral current circuit in quasi-static models of the coupling between the magnetosphere and the auroral ionosphere. Ad hoc profiles of convergent magnetospheric electric fields sustain field-aligned potential differences of the order of several kV and field-aligned current densities of the order of  $\mu\text{A m}^{-2}$  (Lyons, 1980, 1981; Echim et al., 2007; De Keyser and Echim, 2010). Tangential discontinuities (TD) and their associated convergent electric field have been suggested as natural magnetospheric generators for auroral and sub-auroral processes by Roth et al. (1993), De Keyser and Roth (1998), and Echim et al. (2007). De Keyser and Echim (2010) discussed the formation of convergent and divergent magnetospheric electric fields and their auroral and sub-auroral effects. The model developed by Echim et al. (2007, 2008) describes the coupling between auroral arcs and such TD generators located at plasma interfaces formed at the inner edge of the magnetospheric LLBL, in regions close to the terrestrial magnetopause. In this study we adapt this model to describe the coupling between the magnetosphere and the polar ionosphere for the PCIB jointly observed by Cluster and TIMED.

The flux of magnetospheric particles precipitating into the polar cap ionosphere from the magnetospheric generator contributes to a net field-aligned current with a density  $J_{\parallel}$ . The current-voltage relationship (CVR) gives  $J_{\parallel}$  as a function of the field-aligned potential drop,  $\Delta\Phi = \Phi_m - \Phi_i$ , between the generator (described by the electric potential  $\Phi_m$ ) and the polar cap ionosphere (whose electric potential is  $\Phi_i$ ). The CVR has been derived for magnetospheric convergent magnetic fields and for a  $\Delta\Phi$  decreasing monotonically with altitude, by assuming that the motion of particles along the flux tube connecting the generator and the load is adiabatic (Knight, 1973; Lemaire and Scherer, 1973; Chiu and Schulz, 1978; Fridman and Lemaire, 1980; Pierrard, 1996). When the Hall currents are divergence-free, the current continuity equation in the topside polar cap ionosphere requires that the net parallel current in the ionosphere,  $J_{\parallel}$ , is equal to the divergence of the horizontal height-integrated Pedersen current in the ionosphere ( $I_P = \Sigma_P E_i$ ):

$$J_{\parallel} = \frac{d}{dx_i} \left( \Sigma_P \frac{d\Phi_i}{dx_i} \right) \quad (1)$$

where  $J_{\parallel}$  is given by the CVR, a nonlinear function of  $(\Phi_m - \Phi_i)^1$ ;  $x_i$  denotes the distance perpendicular to the arc at ionospheric altitude and  $\Sigma_P(x_i)$  is the height-integrated Pedersen conductivity that depends on the flux of precipitating electrons (Harel et al., 1977). Equation (1) gives a quantitative description of the coupling between the plasma

<sup>1</sup>Note, however, that a linear regime,  $J_{\parallel} = K(\Phi_m - \Phi_i)$  can be identified, both experimentally and theoretically, as shown by Lyons et al. (1979); see also de Keyser and Echim, 2010

and magnetic field properties of the magnetospheric generator and the plasma and field properties of the polar cap arc. Equation (1) is solved for the unknown ionospheric potential  $\Phi_i$  and the input parameters  $\Phi_m$  and  $\Sigma_P$ . The ionospheric feedback effect is introduced in Eq. (1) via the relationship between  $\Sigma_P$  and  $\varepsilon_{em}$ , the energy flux of the precipitating electrons (Harel et al., 1977; Lundin and Sandahl, 1978; see also Echim et al., 2008):

$$\Sigma_P = \Sigma_{P0} + a\sqrt{\varepsilon_{em}} \quad (2)$$

where  $\Sigma_{P0}$  is the base level of the ambient/background Pedersen conductance produced by the solar EUV radiation. In our simulation, we use a relatively high background Pedersen conductance ( $\Sigma_{P0} = 3.5 \Omega^{-1}$ ) in order to simulate the sunlit conditions at the footprint of the magnetic field lines where the PCIB is detected. The variation of conductance due to precipitating electrons does not exceed 20% of the background conductance.

The energy flux of precipitating electrons in the ionosphere<sup>2</sup>,  $\varepsilon_{em}$ , is computed by evaluating the down-going adiabatic motion of electrons in the mirroring magnetic field described by a magnetospheric to ionospheric field ratio  $B_m/B_i$ , and a field-aligned potential drop  $\Delta\Phi = \Phi_i - \Phi_m$ . The magnetic mirror force breaks the field-aligned motion of down-going electrons while a positive  $\Delta\Phi$  will accelerate them downward. From the combined action of the two forces, some electrons will not have enough energy to overpass the magnetic mirror force, some electrons will precipitate in the ionosphere and some electrons may be trapped (see Lemaire and Scherer, 1971, 1973, for details on the characteristics of each class). Assuming that  $\Delta\Phi$  varies monotonically with the altitude  $z$ , the analysis of particle dynamics of each class of electrons and the Liouville mapping of the high-altitude magnetospheric velocity distribution function (VDF) yield the moments of the VDF at each altitude, including in the topside ionosphere. The second-order moment of VDF provides the energy flux of precipitating electrons at ionospheric altitude  $z_i$  as a function of the temperature and density of the magnetospheric source region or generator and the magnetic field mirror ratio (Lundin and Sandahl, 1978):

$$\varepsilon_{em} = N_e k T_e \left( \frac{B_i}{B_m} \right) \sqrt{\frac{k T_e}{2\pi m_e}} \left\{ \left( 2 + \frac{e\Delta\Phi}{k T_e} \right) - \left[ \frac{e\Delta\Phi}{k T_e} + 2 \left( 1 - \frac{B_m}{B_i} \right) \right] e^{-\frac{e\Delta\Phi}{\left( \frac{B_i}{B_m} - 1 \right) k T_e}} \right\} \quad (3)$$

where  $N_e$  and  $T_e$  are the density and temperature of the magnetospheric electrons originating in the magnetospheric generator,  $B_i$ ,  $B_m$  is the magnetic field intensity in the ionosphere and magnetosphere, respectively;  $\Delta\Phi$  is the potential drop between the magnetospheric generator and the polar cap arc.

<sup>2</sup>Equation (2) is, however, valid at any altitude  $z$ , with  $B_i = B(z)$  and  $\Delta\Phi(z) = \Phi(z) - \Phi_m$

The nonlinear Eq. (1) is discretized using a finite difference method and integrated numerically with a damped Newton iterative scheme and Dirichlet boundary conditions. In Eq. (1)  $J_{\parallel}$  is given by the CVR where we introduce  $\Phi_m$ , the magnetospheric electric potential, from electric field measurements by Cluster 1 at  $z_m = 5.5 R_E$  (see Fig. 5). The density and temperature of magnetospheric electrons and ions are also provided by Cluster 1 measurements and introduced in Eqs. (1)–(3). Equation (1) is then solved for  $\Phi_i$ , the ionospheric potential at an altitude of 500 km. The current carried by ionospheric electrons and ions is also included in Eq. (1) using analytical expressions derived by Lemaire and Scherer (1971). Note that we use as a boundary condition  $J_{\parallel} = 0$  at both sides of the PCIB and we model only the upward current region ( $J_{\parallel} = 0$  when  $\Delta\Phi < 0$ ).

From the condition that the magnetic flux is conserved and assuming a cylindrical mapping (Lyons, 1980), the distance  $x_m$ , at the magnetospheric altitude  $z_m$  where the magnetic field is  $B_m$  maps to  $x_i$  at the ionospheric altitude  $z_i$ , where the magnetic field is  $B_i$ , according to the relationship  $x_i = x_m \sqrt{B_m/B_i}$ . The ionospheric electric potential obtained from Eq. (1) provides implicitly the field-aligned potential drop  $\Delta\Phi$  which is introduced back in the analytical expression of  $J_{\parallel}$ ,  $\varepsilon_{em}$ , and  $\Sigma_P$  at the ionospheric altitude  $z_i$ . The results of the MI coupling model are summarized in Fig. 9. Thus, our MI coupling model provides an estimation of the electrodynamic properties of the polar cap arc coupled to the convergent electric field and the associated PCIB observed by Cluster.

In order to estimate the optical emission rates that would correspond to the accelerating potential  $\Delta\Phi$  resulting from the MI coupling model adapted for PCA and to compare these emission rates with the direct observations by TIMED, we compute an electron differential energy flux precipitating into the polar cap ionosphere. We take a Maxwellian electron velocity distribution function at the altitude of Cluster and inject it into the field-aligned potential drop  $\Delta\Phi$  inferred from solving Eq. (1) subject to Eqs. (2)–(3). The Maxwellian is defined such that its density profile ( $N_e(x_m)$ ) and temperature ( $T_e = 120$  eV) are consistent with Cluster observations. Note that the field-aligned acceleration above Cluster is not taken into account as we have no information on its altitude distribution. However, this may only slightly impact the results as it represents a small fraction of the total field-aligned potential drop (less than 25%). This electron VDF is then Liouville mapped at ionospheric altitudes where we compute the resulting spectrum of the differential energy flux. The result shown in Fig. 9 is in good agreement, in terms of spatial scale, with observations of PCIB by Cluster and with optical observations of the PCA by TIMED-GUVI. The ionospheric potential is relatively linear as because the field-aligned currents are relatively low and ionospheric conductivity high. Therefore, the field-aligned potential drop  $\Delta\Phi$  is rather similar to the magnetospheric potential  $\Phi_m$  measured by Cluster.

The magnetosphere and ionosphere are, thus, decoupled by field-aligned electric fields confirming that the strong perpendicular electric field observed by Cluster on the sides of the PCIB is converted into field-aligned electric field at lower altitude. Consequently, the PCIB is not expected to be associated with strong perpendicular electric fields at ionospheric altitudes.

The energy spectrum of precipitating electrons computed from this MI coupling model is then used as an input variable for the TRANS4 model that computes the corresponding emission rates to be compared with emission rates from TIMED-GUVI data.

#### 4.2 Ionospheric response: modelling the optical emissions

The spin-forbidden transition  $O(3s^5S^o-2p^3P)$  emits a doublet in the FUV at 135.6 nm and 135.8 nm, usually appearing as one line in space-borne and ground-based instruments. It is excited exclusively by electron impact (e.g. Anderson et al., 1980; Avakyan, 1998) and can be considered optically thin when observed in nadir configuration (Strickland and Anderson, 1983; Germany et al., 1990). Extinction due to absorption by  $O_2$  molecules in the Schumann-Runge continuum is important between 100 and 150 km altitude where  $O_2$  is the predominant species (Meier, 1991). Contamination by the  $N_2(a^1\Pi_g-X^1\Sigma_g^+)$  LBH (3,0) band at 135.4 nm may also occur, especially in the bottom-side of the atmosphere, as explained in Meier et al. (1985) and reaches 8 to 20 % of the overall emission at 200 km altitude depending on solar and atmospheric conditions.  $O^+-O^-$  neutralization may also play a role (around 5 % of the total emission), especially in the mid-latitude ionosphere (Meier, 1991; Dymond et al., 2000) and at low altitudes. These two last mechanisms as well as cascades from  $^5P$  upper states (Kanik et al., 2003) will not be considered here as a lower estimate is sought. The sources of excitation considered here are:

- $O + e \rightarrow O^* + e$ : electron impact excitation (a)
- $O_2 + e \rightarrow O^* + O^* + e$ : electron impact dissociative excitation (b)
- $O^+ + e \rightarrow O^* + h\nu$  (135.6 nm): radiative recombination (c)
- $N_2 + e \rightarrow N_2^* + h\nu$  (135.4 nm): contamination from LBH band at 135.4 nm (d)

Processes (a) and (b) contribute to more than 85 % of the total brightness (Strickland and Anderson, 1983; Strickland et al., 1993) and processes (c) and (d) to around 10 % or less (Dymond et al., 2000, and this study). As electron recombination is mostly important on the nightside, the knowledge of the electron and ion densities is needed, hence the use of a fluid ionospheric model.

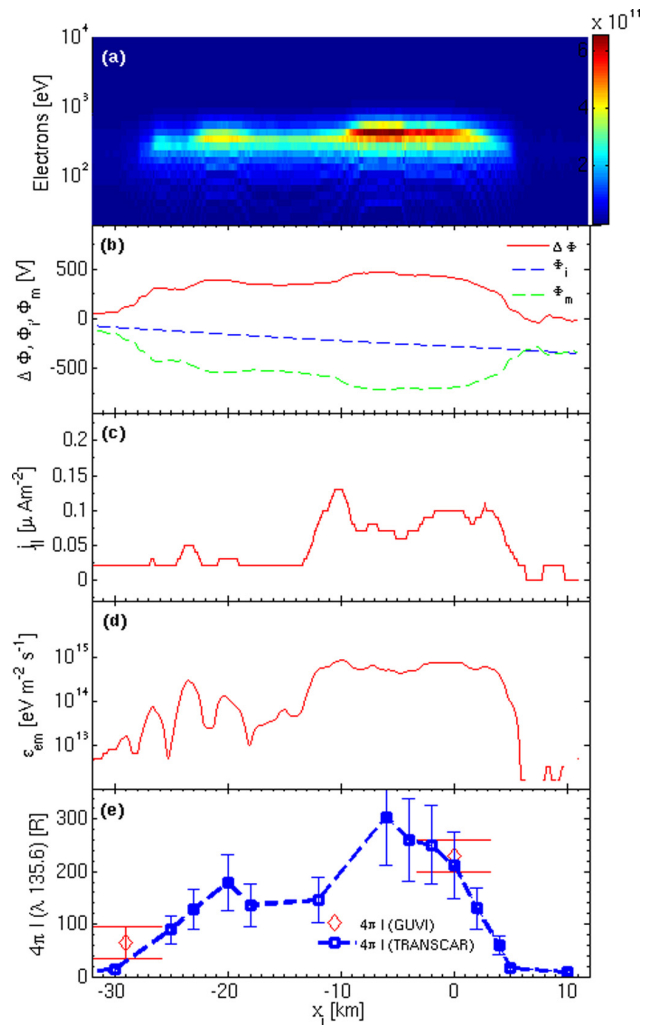


**Fig. 9.** Results of the MI coupling model. from top to bottom: (first panel) synthetic energy spectrum of precipitating electrons at 500 km; this spectrum is obtained by injecting a Maxwellian distribution function into the field-aligned potential difference,  $\Delta\Phi$ , illustrated in the second panel,  $\Delta\Phi$  results from solving the current continuity Eq. (1) for  $\Phi_m$ , the magnetospheric electric potential, given by Cluster measurements at an altitude of  $5.5 R_E$ ; the third panel illustrates the field-aligned current density given by the CVR for the computed  $\Delta\Phi$ ; the fourth panel shows the energy flux of precipitating electrons, computed from Eq. (3). The last panel displays the emission profile at 135.6 nm as computed from our simulation and as measured by TIMED. The shape and intensities computed are consistent with the given input spectra and the brightness spatial distribution recorded by GUVI.

To compute the production of  $O(^5S^o)$  taking into account all channels, a 1-D coupled kinetic-fluid electron transport model, called TRANS4 (Simon et al., 2007), is used. A simplified synopsis is shown in Fig. 8. TRANS4 solves the 1-D Boltzmann equation for superthermal electrons, taking into account photoionization, photoexcitation and electron transport of photoelectrons and precipitated electron (following

Lilensten et al., 1989), so that the superthermal electron flux  $\Phi_e$ , depending on the altitude  $z$ , the energy  $E$  and the cosine of the electron pitch angle  $\mu$ , is expressed by:

$$\mu \frac{\partial}{\partial z} \varphi_e(z, E, \mu) - n_e \frac{\partial}{\partial E} (L(E) \varphi_e(z, E, \mu)) = C(\varphi_e(z, E, \mu)) \quad (4)$$

Where  $L(E)$ , in  $\text{eV cm}^{-2}$ , is the loss function describing the dissipative friction between thermalized and superthermal electrons in the approximation of continuous slowing down (CSDA).  $n_e$  is the electron density in  $\text{cm}^{-3}$ .  $C(\varphi_e)$  is the collision operator including direct sources of superthermal electrons (photon, electron or proton impact) and sources and losses of electrons by collisions with the environment.

Among sources, photoabsorption is computed using a Beer-Lambert law while electron precipitation is directly calculated from the precipitation differential fluxes (in  $\text{cm}^{-2} \text{s}^{-1} \text{eV}^{-1}$ ), either measured by satellites or given by an external model such as the one described in Sect. 4.1.

The fluid module includes a 8-moment approximation coupled to the kinetic module and computes electron and ion densities of  $\text{N}_2^+$ ,  $\text{O}_2^+$ ,  $\text{O}^+$ ,  $\text{N}^+$ ,  $\text{NO}^+$  and  $\text{H}^+$  (Lilensten and Blelly, 2002). The neutral atmosphere is given by the semi-empirical model MSIS-90 (Hedin, 1991) and the solar EUV flux is given by the solar model EUVAC (Richards et al., 1994a, b) with the 37 energy boxes of Torr and Torr (1985) modified to take into account higher energies. MSIS-90 and EUVAC are parameterized in the present study by the decimetric solar index  $F_{10.7}$ . Photoabsorption, ionization and electron impact excitation and ionization cross-sections are, for instance, described in Lilensten and Blelly (2002) and Simon et al. (2007) and references therein.

Prominent auroral emissions such as OI (557.7 nm), OI (630.0 nm) or OI (135.6 nm) are directly computed from the production rate of excited states (expressed in  $\text{cm}^{-3} \text{s}^{-1}$ ):

$$P_{\text{emi}}^j(z) = n_j(z) \int \sigma_{\text{emi}}^j(E) \varphi_e(z, E) dE \quad (5)$$

Where  $n_j$  is the density of the parent neutral species  $j$ ,  $\sigma_{\text{emi}}^j$  is the excitation or emission cross section from neutral species  $j$ . In the case of OI (135.6), the two channels (a)–(b) are included in the model in this manner.

The most recent cross-sections for processes (a) and (b) used in the computation are Laher and Gilmore (1990) and Kanik et al. (2003), respectively. The recommendation of Laher and Gilmore (1990) for process (a), deduced from calculations, is in qualitative agreement with the laboratory measurements reported by Stone and Zipf (1974), later corrected by Zipf and Erdman (1985) and Doering and Gulcicek (1989); the uncertainty reaches 50%. At 70 eV energy, process (b) is around 50 times less efficient than process (a). Emission cross-sections for process (d), i.e.  $\text{N}_2$  LBH (0,3) emission at 135.4 nm, are initially taken from Ajello and Shemansky (1985) multiplied by 0.892 as recommended by Itikawa (2006).

Radiative recombination process (c) is included directly by calculating the emission rate:

$$P_{135.6}^{\text{O}^+}(z) = k_r n_e(z) n_{\text{O}^+}(z) \quad (6)$$

where  $n_e$  and  $n_{\text{O}^+}$  are the electron density and  $\text{O}^+$  ion density, respectively, both calculated by the fluid part of the TRANS4 model.  $k_r$  is the recombination coefficient equal to  $7.3 \times 10^{-13} \text{cm}^3 \text{s}^{-1}$  for an electron temperature  $T_e = 1160 \text{K}$  as given by Meléndez-Alvira et al. (1999a, b).

The total volume emission rate  $\eta_{135.6}$  including the contamination from LBH (3,0) band is:

$$\eta_{135.6}(z) = \sum_{j=\text{O}_2, \text{O}} P_{135.6}^j(z) + P_{135.6}^{\text{O}^+}(z) + P_{135.4}^{\text{N}_2}(z) \quad (7)$$

In order to compare to the nadir-pointing GUVI observations, the volume emission rates are integrated along the vertical line of sight (nadir mode) and converted into Rayleigh units of intensity  $I$ , following the definition of Hunten et al. (1956) ( $1 \text{R} = 10^6 \text{photons cm}^{-2} \text{s}^{-1}$ ). Adding the reabsorption of 135.6 nm photons by  $\text{O}_2$  molecules, significant at the altitude of the emission peak, the integration becomes in Rayleigh:

$$4\pi I = \int \eta_{135.6}(z) e^{-\sigma_{\text{hv}}^{\text{O}_2}(\lambda=135.6 \text{nm}) \int n_{\text{O}_2}(z') dz'} dz \quad (8)$$

Where  $\sigma_{\text{hv}}^{\text{O}_2}$  ( $\lambda = 135.6 \text{nm}$ ) is the value of the photoabsorption cross-section of  $\text{O}_2$  at 135.6 nm, measured at  $7.24 \times 10^{-18} \text{cm}^2$  by Yoshino et al. (2005).

The conditions of the TIMED-GUVI observations are nadir-pointing for the middle of the arc on 1 April 2004, 06:44 UT, geographic latitude/longitude ( $81^\circ \text{N}$ ,  $54^\circ \text{W}$ ),  $F_{10.7} = 112$  and a solar zenith angle equal to  $86^\circ$ . The corresponding neutral atmosphere is given by MSIS-90. Following Gattinger et al. (1996), atomic oxygen densities are within the range  $0.75 \pm 0.25$  of MSIS-90 original density to account for high-latitude thermospheric conditions. Input electron fluxes are computed by the MI model described in Sect. 4.1, with the following relation between electron velocity distribution function  $f_e(v_{\parallel}, v_{\perp}, \mu)$  at the top of the ionosphere in  $\text{cm}^{-6} \text{s}^3$  and the corresponding particle differential flux  $\Phi_e$  in  $\text{cm}^{-2} \text{s}^{-1} \text{eV}^{-1}$  (Baumjohann and Treumann, 1997):

$$\Phi_e(E, \mu) = \frac{v^2}{m_e} f_e(v_{\parallel}, v_{\perp}, \mu) \quad (9)$$

Where  $v_{\parallel}$  and  $v_{\perp}$  are the velocities parallel and perpendicular to the magnetic field  $\mathbf{B}$ . Another output of the TRANS4 model is the Pedersen conductance. In the middle of the arc the integrated Pedersen conductance given by TRANS4 is  $3.5 \pm 0.5 \Omega^{-1}$  which is similar to the empirical value used in the MI model.

### 4.3 Comparison between the modelled emissions and TIMED observations

Modelling results are shown in Fig. 9 where the emission profile at nadir measured by TIMED is also plotted. The profile of emission across the structure displays a plateau in the

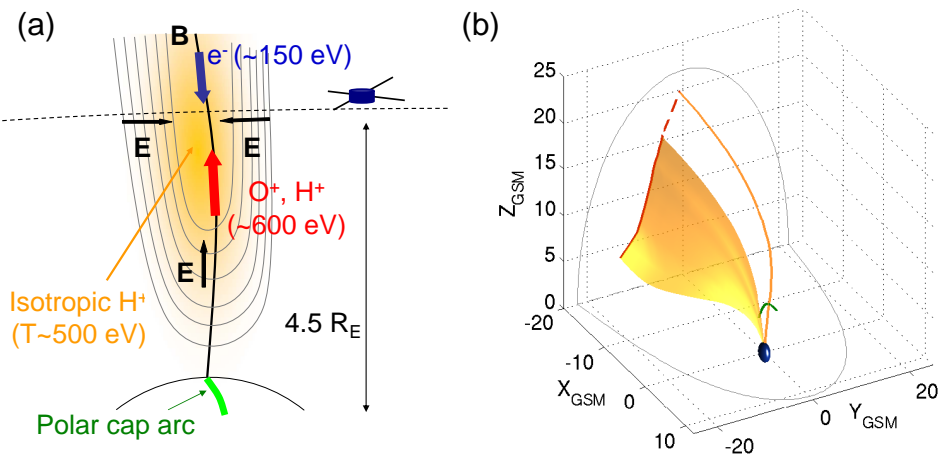


**Fig. 10.** (a) Sketch summarizing Cluster observations on 1 April 2004. The particle populations detected by the spacecraft are indicated together with the electric field topology. According to our modelling, such structure should create optical emissions at ionospheric altitude. (b) Schematic plot of the magnetosphere on 1 April 2004. The grey dotted line shows the location of the magnetopause according to the Shue et al. (1997) model in the  $XY_{\text{GSM}}$  and  $YZ_{\text{GSM}}$  planes. The green line represents Cluster 1 orbit from 04:40 UT to 08:25 UT. The orange line shows the magnetic field line passing by Cluster 1 when it detects the inverted-V structure. The orange surface is a mapping along the magnetic field lines of the polar cap arc detected by TIMED. The red line shows the intersection between this surface and the  $X_{\text{GSM}} = -20 R_E$  plane. It is extended by a red dotted line which connects it to the magnetic field line passing by Cluster 1 when it detects the inverted-V structure. The mapping is made using the Tsyganenko 2004 model (Tsyganenko and Sitnov, 2005).

centre with a maximum intensity of about 250 R with uncertainties of around  $\pm 25\%$  as derived in Gronoff et al. (2012). On the sides the intensity sharply decreases and the width at half maximum intensity from our simulation is about 30 km. This is in good agreement with the values recorded by the Global Ultraviolet Imager (GUVI) onboard TIMED (respectively  $\sim 230$  R and 37 km).

Simulations show that processes (a) and (b) contribute to more than 49% each of the total calculated intensity, while radiative recombination is a minor process (less than 1%).  $\text{O}_2$  reabsorption decreases the total intensity by around 2% in nadir configuration.

Furthermore, the simulations show that the two thin and low energetic ion beams detected around 06:18 UT and 06:22 UT are not likely to produce emissions corresponding to the arc measured by TIMED. First, their width at ionospheric altitude (estimated to less than 10 km) is much lower than the width of the polar cap arc. Second, they are not energetic enough to produce intense emissions. Indeed we can barely estimate it with the intensity observed on the sides of the PCIB where the upflowing ion energy is of  $\sim 100$  eV. The corresponding intensity at 135.6 nm should be lower than  $\sim 50$  R which is well beyond the intensity of the polar cap arc according to GUVI data.

## 5 Summary and discussion

In this study, we compared observations from Cluster and TIMED above the Northern polar cap during a prolonged period of northward IMF. During this time period, the GUVI

imager onboard TIMED detects a polar cap arc in the polar cap ionosphere, and 20 min later, the Cluster spacecraft detect an upflowing ion beam with an inverted-V structure. Panel (a) of Fig. 10 summarizes Cluster observations of the PCIB. Due to their relatively high altitude, the Cluster spacecraft spent a long time inside it and, thus, received detailed observations of the particle and fields. Cluster data show clear evidence that the upgoing ions are accelerated by a quasi-static electric field with U-shaped equipotentials. Such outflow structures are frequently detected by Cluster above the polar caps during prolonged periods of northward IMF (Maggiolo et al., 2011) and are named polar cap ion beams (PCIB).

The PCIB detected by Cluster maps outside the GUVI field-of-view data analysis and modelling, however, reveal similarities with the polar cap arc observed by TIMED. Therefore, we conjecture that they are both different signatures of the same phenomenon.

A direct confirmation comes from the modelling of  $\Delta\Phi$ , the field-aligned potential drop and the corresponding UV emission rates. We developed a method based on two complementary models: (A) a quasi-stationary MI coupling model based on the current continuity (1) and a kinetic current-voltage relationship, a model initially developed for discrete arcs in the main auroral oval, and (B) a kinetic model for computing the emission rates corresponding to the flux of precipitating energy determined from model (A). Electric field measurements by Cluster in the upper segment of the acceleration region provide the magnetospheric electric potential profile,  $\Phi_m$ . The latter is introduced into the MI

coupling model that provides,  $\Delta\Phi$ , the potential drop between the magnetosphere and the polar cap ionosphere.

In order to estimate the precipitating energy flux in the polar cap ionosphere, we “launch” electrons with a Maxwellian distribution function with a temperature and density as given by Cluster measurements. The Liouville mapping of this VDF through the field-aligned potential drop computed by MI coupling model gives the spectrum of precipitating electrons at ionospheric altitude. This spectrum is then used as input to a kinetic airglow model to compute the emission profile at a given wavelength. We applied this method to the PCIB using Cluster data as input and compared the modelled emissions to the polar cap emission as measured by TIMED focusing on the OI line at 135.6 nm. The spatial scale of the field-aligned potential structure and the maximum of  $\Delta\Phi$  are in good agreement with Cluster observations of the PCIB. The modelled emission profile computed at ionospheric altitudes also shows good agreement with the emission rates measured by GUVI. Thus, experimental and modelling results suggest that Cluster and TIMED-GUVI observed the same phenomenon, an elongated polar cap arc with a width of the order of 30 km and which extends virtually over the entire polar cap. The polar cap arc brightness is of the order of 250 R, consistent with model results, and the arc is stable over a time interval of the order of tens of minutes. The modelling results suggest that the mechanism sustaining the polar cap arc and its associated ion upflows is quasi-static, similar to the quasi-static acceleration in the auroral oval.

It has been already shown that PCIB have statistical properties similar to polar cap arcs (Maggiolo et al., 2011). Based on simultaneous in situ and optical data, we confirm in this study that the PCIB observed by Cluster is likely to be a high-altitude signature of the polar cap arc imaged by TIMED. We can, therefore, conjecture that PCIB and polar cap arcs are different signatures of the same phenomenon, hallmark of magnetospheric dynamics during prolonged periods of Northward IMF.

We can, thus, combine Cluster and TIMED measurements to get a better understanding of the magnetospheric configuration during this event. Cluster gives a detailed description of the PCIB electrodynamic at high altitude. In particular, it reveals the presence of a population of warm ( $\sim 500$  eV) and tenuous ( $\sim 0.002$  cm $^{-3}$ ) ions located inside the quasi-static acceleration region. Such plasma population is associated with 40 % of PCIB (Maggiolo et al., 2011). The presence of isotropic plasma filaments in the lobe regions during periods of northward IMF has been previously reported, for example, by Interball (e.g. Grigorenko et al., 2002), ISEE (e.g. Huang et al., 1987) or Cluster (e.g. Petrukovich et al., 2003). However, the spatial coverage of spacecraft measurement is limited and inadequate to infer the large scale geometry of these filaments. With the method presented in this study, we relate Cluster high altitude observations to optical emissions at the ionospheric level and overcome the limited coverage of in situ observations. The GUVI image provides a large scale

outlook of the polar cap arc spatial structure that we can combine with Cluster data to infer magnetospheric configuration (see Fig. 10b). If, as suggested by the GUVI image, the properties of the polar cap arc do not vary along it, the polar cap arc imaged by GUVI should be associated with a curtain-like sheet of warm isotropic ions located inside the magnetospheric lobes. This sheet, represented in orange in Fig. 10b, also corresponds to the region of upward current associated with the precipitating electrons and upflowing ions measured by Cluster. This sheet is thin (about 300 km at an altitude of  $4.5 R_E$ ) and extends approximately along the  $Z_{GSM}$  axis in the magnetotail. The polar cap arc detected by TIMED is connected to the auroral oval in the nightside and, thus, this sheet should be connected to the plasmashet. There is no asymmetry between the magnetospheric regions located on the two sides of this sheet. The convection is weak and directed sunward and they are populated by cold plasma with a density of about 0.2–0.4 cm $^{-3}$ , typical of open magnetic field lines of the lobe region.

The configuration of the magnetic field lines on which the PCIB are detected is not standard and the topology of these field lines cannot be directly inferred from Cluster measurements (see Maggiolo et al., 2011). The presence of warm isotropic ions favours a closed field line configuration. However, these ions are detected only for 40 % of PCIB and in this particular event only on one side of the PCIB. On the other hand, the low temperature of precipitating electrons associated with PCIB and the fact that PCIB are very thin structures located at high latitude in the magnetospheric lobes would suggest an open field line configuration. This issue goes beyond the scope of this paper and will be addressed in dedicated studies.

The quantitative analysis of the PCIB and its associated field-aligned potential drop, as well as the successful modelling of the optical emission rates opens new possibilities for exploitation of in situ spacecraft data for a better understanding of polar cap arcs. The information we get about the magnetospheric configuration and the local electrodynamic are useful to test polar cap arcs formation models. It can also be applied to other spacecraft, for instance low-altitude spacecraft like DMSP for which the energy spectrum of precipitating electrons can directly be obtained from measurements. This possibility can be explored in the future by investigating additional conjunctions between in situ spacecraft measurements and polar imagers.

Furthermore, the method described in this paper developed to compute the optical emission rates in polar cap arcs from particle and fields observations can give an estimate of the visibility condition for polar cap arcs. Simulating optical emissions would be helpful to confront optical data with in situ measurements avoiding possible bias due to the imagers’ sensitivity. Indeed, smaller field-aligned potential drops would produce fainter emissions and, therefore, unlikely to be observed by ground-based or space imagers. This may be particularly useful for the study of polar cap arcs

and PCIB which are associated with precipitating electrons of relatively low energy (e.g. Whalen et al., 1971; Hardy et al., 1982; Maggiolo et al., 2011).

*Acknowledgements.* The authors are grateful to E. Penou for the development of CL, the Cluster CIS software, to the Cluster Active Archive for providing Cluster data and to the CDAWEB for providing ACE data. R. Maggiolo is supported by a PRODEX/CLUSTER contract (PEA 90096). M. Echim acknowledges support from the Belgian Office for Science (BELSPO) grant MO/35/031 and from ESA PECS grant 98049/2007. C. Simon Wedlund is supported by the Belgian BELSPO-PPS Science Policy through the Action 1 contract MO/35/019 and MO/35/025. The authors are also acknowledging the AtMoCIAD data base. C. S. W. is deeply indebted to G. “42” Gronoff (NASA Langley RC, VA, USA) and to J. Lilénsten (IPAG, France) for numerous discussions about updated cross-sections, the airglow model, the associated uncertainties and the calculation of ionospheric conductivities.

Guest Editor M. Taylor thanks two anonymous referees for their help in evaluating this paper.

## References

- Ajello, J. M. and Shemansky, D. E.: A reexamination of important  $N_2$  cross sections by electron impact with application to the dayglow – The Lyman-Birge-Hopfield band system and N I (1199.99 nm), *J. Geophys. Res.*, 90, 9845–9861, 1985.
- Anderson Jr., D. E., Meier, R. R., Feldman, P. D., and Gentieu, E. P.: The UV dayglow 3, OI emissions at 989, 1027, 1152, 1304, and 1356 Å, *Geophys. Res. Lett.*, 7, 1057–1060, 1980.
- Avakyan, S. V. (Ed.): Collision processes and excitation of UV emission from planetary atmospheric gases: a handbook of cross sections, Gordon and Breach Science Publishers, Amsterdam, The Netherlands, 1998.
- Balogh, A., Carr, C. M., Acuña, M. H., Dunlop, M. W., Beek, T. J., Brown, P., Fornacon, K.-H., Georgescu, E., Glassmeier, K.-H., Harris, J., Musmann, G., Oddy, T., and Schwingenschuh, K.: The Cluster Magnetic Field Investigation: overview of in-flight performance and initial results, *Ann. Geophys.*, 19, 1207–1217, doi:10.5194/angeo-19-1207-2001, 2001.
- Baumjohann, W. and Treumann, R. A.: Basic space plasma physics, London: Imperial College Press, 1997.
- Berg, G. A., Kelley, M. C., Mendillo, M., Doe, R., Vickrey, J., Kletzing, C., Prindahl, F., and Baker, K. D.: Formation and eruption of Sun-aligned arcs at the polar cap-auroral oval boundary, *J. Geophys. Res.*, 99, 17577–17589, 1994.
- Bonnell, J., Elphic, R. C., Palfery, S., Strangeway, R. J., Peterson, W. K., Klumpar, D., Carlson, C. W., Ergun, R. E., and McFadden, J. P.: Observations of polar cap arcs on FAST, *J. Geophys. Res.*, 104, 12669–12682, 1999.
- Burke, W. J., Hardy, D. A., Rich, F. J., Gussenhoven, M. S., and Kelley, M. C.: Electric and magnetic field characteristics of discrete arcs in the polar cap, *J. Geophys. Res.*, 87, 2431–2443, 1982.
- Carlson, H. C. and Cowley, S. W. H.: Accelerated polar rain electrons as the source of Sun-aligned arcs in the polar cap during northward interplanetary magnetic field conditions, *J. Geophys. Res.*, 110, A05302.1–A05302.10, 2005.
- Carlson, H. C., Weber, E. J., Heelis, R. A., and Sharber, J. R.: Coherent mesoscale convection patterns during northward interplanetary magnetic field, *J. Geophys. Res.*, 93, 14501–14514, 1988.
- Chiu, Y. T. and Schulz, M.: Self-consistent particle and parallel electrostatic field distributions in the magnetospheric-ionospheric auroral region, *J. Geophys. Res.*, 83, 629–642, 1978.
- Christensen, A. B., Paxton, L. J., Avery, S., Craven, J., Crowley, G., Humm, D. C., Kil, H., Meier, R. R., Meng, C.-I., Morrison, D., Ogorzalek, B. S., Straus, P., Strickland, D. J., Swenson, R. M., Walterscheid, R. L., Wolven, B., and Zhang, Y.: Initial observations with the Global Ultraviolet Imager (GUVI) in the NASA TIMED satellite mission, *J. Geophys. Res.*, 108, SIA 16-1, 2003.
- Décrou, P. M. E., Fergeau, P., Krasnoselskikh, V., Le Guirrec, E., Lévêque, M., Martin, Ph., Randriamboarison, O., Rauch, J. L., Sené, F. X., Séran, H. C., Trotignon, J. G., Canu, P., Cornilleau, N., de Féraudy, H., Alleyne, H., Yearby, K., Mgensen, P. B., Gustafsson, G., André, M., Gurnett, D. C., Darrouzet, F., Lemaire, J., Harvey, C. C., Travnicek, P., and Whisper experimenters: Early results from the Whisper instrument on Cluster: an overview, *Ann. Geophys.*, 19, 1241–1258, doi:10.5194/angeo-19-1241-2001, 2001.
- De Keyser, J. and Echim, M.: Auroral and sub-auroral phenomena: an electrostatic picture, *Ann. Geophys.*, 28, 633–650, doi:10.5194/angeo-28-633-2010, 2010.
- De Keyser, J. and Roth, M.: Equilibrium conditions and magnetic field rotation at the tangential discontinuity magnetopause, *J. Geophys. Res.*, 103, 6653–6662, 1998.
- De Keyser, J., Maggiolo, R., and Echim, M.: Monopolar and bipolar auroral electric fields and their effects, *Ann. Geophys.*, 28, 2027–2046, doi:10.5194/angeo-28-2027-2010, 2010.
- Doering, J. P. and Gulcicek, E. E.: Absolute differential and integral electron excitation cross sections for atomic oxygen. VIII – The  $^3P - ^5S^0$  transition (1356 Å) from 13.9 to 30 eV, *J. Geophys. Res.*, 94, 2733–2736, 1989.
- Dymond, K. F., McCoy, R. P., Thonnard, S. E., Budzien, S. A., Thomas, R. J., Bullett, T. N., and Bucsel, E. J.: O<sup>+</sup>, O, and O<sub>2</sub> densities derived from measurements made by the High Resolution Airglow/Aurora Spectrograph (HIRAAS) sounding rocket experiment, *J. Geophys. Res.*, 105, 23025–23034, 2000.
- Echim, M. M., Roth, M., and De Keyser, J.: Sheared magnetospheric plasma flows and discrete auroral arcs: a quasi-static coupling model, *Ann. Geophys.*, 25, 317–330, doi:10.5194/angeo-25-317-2007, 2007.
- Echim, M. M., Roth, M., and De Keyser, J.: Ionospheric feedback effects on the quasi-stationary coupling between LLBL and post-noon/evening discrete auroral arcs, *Ann. Geophys.*, 26, 913–928, doi:10.5194/angeo-26-913-2008, 2008.
- Engwall, E., Eriksson, A. I., Cully, C. M., André, M., Puhl-Quinn, P. A., Vaith, H., and Torbert, R.: Survey of cold ionospheric outflows in the magnetotail, *Ann. Geophys.*, 27, 3185–3201, doi:10.5194/angeo-27-3185-2009, 2009.
- Eriksson, S., Provan, G., Rich, F. J., Lester, M., Milan, S. E., Masetti, S., Gosling, J. T., Dunlop, M. W., and Rème, H.: Electrodynamics of a split-transpolar aurora, *J. Geophys. Res.*, 111, A11319, doi:10.1029/2006JA011976, 2006.
- Escoubet, C. P., Fehringer, M., and Goldstein, M.: Introduction The Cluster mission, *Ann. Geophys.*, 19, 1197–1200, doi:10.5194/angeo-19-1197-2001, 2001.

- Frank, L. A., Craven, J. D., Burch, J. L., and Winningham, J. D.: Polar views of the earth's aurora with Dynamics Explorer, *Geophys. Res. Lett.*, 9, 1001–1004, 1982.
- Frank, L. A., Craven, J. D., Gurnett, D. A., Shawhan, S. D., Burch, J. L., Winningham, J. D., Chappell, C. R., Waite, J. H., Maynard, N. C., and Sugiura, M.: The theta aurora, *J. Geophys. Res.*, 91, 3177–3224, 1986.
- Fridman, M. and Lemaire, J.: Relationship between auroral electron fluxes and field-aligned electric potential differences, *J. Geophys. Res.*, 85, 664–670, 1980.
- Gattinger, R. L., Llewellyn, E. J., and Vallance Jones, A.: On I(5577 Å) and I (7620 Å) auroral emissions and atomic oxygen densities, *Ann. Geophys.*, 14, 687–698, doi:10.1007/s00585-996-0687-1, 1996.
- Germany, G. A., Torr, M. R., Richards, P. G., and Torr, D. G.: The dependence of modelled OI 1356 and N<sub>2</sub> Lyman Birge Hopfield auroral emissions on the neutral atmosphere, *J. Geophys. Res.*, 95, 7725–7733, 1990.
- Grigorenko, E. E., Fedorov, A., and Zelenyi, L. M.: Statistical study of transient plasma structures in magnetotail lobes and plasma sheet boundary layer: Interball-1 observations, *Ann. Geophys.*, 20, 329–340, doi:10.5194/angeo-20-329-2002, 2002.
- Gronoff, G., Simon Wedlund, C., Mertens, C. J., and Lillis, R. J.: Computing uncertainties in thermosphere-ionosphere-airglow models. I – Electron flux and specie production uncertainties, *J. Geophys. Res.*, submitted, 2012.
- Gussenhoven, M. S. and Mullen, E. G.: Simultaneous relativistic electron and auroral particle access to the polar caps during interplanetary magnetic field B(z) northward – A scenario for an open field line source of auroral particles, *J. Geophys. Res.*, 94, 17121–17132, 1989.
- Haaland, S. E., Paschmann, G., Förster, M., Quinn, J. M., Torbert, R. B., McIlwain, C. E., Vaith, H., Puhl-Quinn, P. A., and Kletzing, C. A.: High-latitude plasma convection from Cluster EDI measurements: method and IMF-dependence, *Ann. Geophys.*, 25, 239–253, doi:10.5194/angeo-25-239-2007, 2007.
- Hardy, D. A., Burke, W. J., and Gussenhoven, M. S.: DMSP optical and electron measurements in the vicinity of polar cap arcs, *J. Geophys. Res.*, 87, 2413–2430, 1982.
- Harel, M., Wolf, R., Reiff, P., and Hillis, H.: Study of plasma flow near the Earth's plasmapause, Tech. Rep. AFGl-TR-77-286, U.S. Air Force Geophys. Lab, 1977.
- Hedin, A. E.: Extension of the MSIS thermosphere model into the middle and lower atmosphere, *J. Geophys. Res.*, 96, 1159–1172, 1991.
- Hoffman, R. A., Heelis, R. A., and Prasad, J. S.: A sun-aligned arc observed by DMSP and AE-C, *J. Geophys. Res.*, 90, 9697–9710, 1985.
- Hosokawa, K., Moen, J. I., Shiokawa, K., and Otsuka, Y.: Motion of polar cap arcs, *J. Geophys. Res.*, 116, A01305, doi:10.1029/2010JA015906, 2011.
- Huang, C. Y., Frank, L. A., Peterson, W. K., Williams, D. J., Lennartsson, W., Mitchell, D. G., Elphic, R. C., and Russell, C. T.: Filamentary structures in the magnetotail lobes, *J. Geophys. Res.*, 92, 2349–2363, 1987.
- Huang, K., McEwen, D. J., and Oznovich, I.: Analysis of a polar auroral arc observed from Eureka (89 deg N) and by DMSP satellites on December 14, 1990, *J. Geophys. Res.*, 99, 21353–21359, 1994.
- Humm, D. C., Paxton, L. J., Christensen, A. B., Ogorzalek, B. S., Pardoe, C. T., Meng, C.-I., Morrison, D., Strickland, D. J., Evans, J. S., Weiss, M. B., Crain, W., Lew, P. H., Mabry, D. J., Goldsten, J. O., Gary, S. A., Peacock, K., Persons, D. F., Harold, M. J., Alvarez, E. B., and Ercol, C. J.: Design and performance of the Global Ultraviolet Imager (GUVI), *Proc. SPIE*, 3445, 2–12, 1998.
- Hunten, D. M., Roach, F. E., and Chamberlain, J. W.: A photometric unit for the airglow and aurora, *J. Atmos. Terr. Physics*, 8, 345–346, 1956.
- Ismail, S. and Meng, C.-I.: A classification of polar cap auroral arcs, *Planet. Space Sci.*, 30, 319–330, 1982.
- Ismail, S., Wallis, D. D., and Cogger, L. L.: Characteristics of polar cap sun-aligned arcs, *J. Geophys. Res.*, 82, 4741–4749, 1977.
- Itikawa, Y.: Cross Sections for Electron Collisions with Nitrogen Molecules, *J. Phys. Chemical Reference Data*, 35, 31, 2006.
- Johansson, T., Marklund, G., Karlsson, T., Liléo, S., Lindqvist, P.-A., Marchaudon, A., Nilsson, H., and Fazakerley, A.: On the profile of intense high-altitude auroral electric fields at magnetospheric boundaries, *Ann. Geophys.*, 24, 1713–1723, doi:10.5194/angeo-24-1713-2006, 2006.
- Johnstone, A. D., Alsop, C., Burge, S., Carter, P. J., Coates, A. J., Coker, A. J., Fazakerley, A. N., Grande, M., Gowen, R. A., Gurgiolo, C., Hancock, B. K., Narheim, B., Preece, A., Sheather, P. H., Winningham, J. D., and Woodliffe, R. D.: PEACE, A Plasma Electron And Current Experiment, *Space Sci. Rev.*, 79, 351–398, 1997.
- Kanik, I., Noren, C., Makarov, O. P., Vattipalle, P., Ajello, J. M., and Shemansky, D. E.: Electron impact dissociative excitation of O<sub>2</sub>: 2. Absolute emission cross sections of the OI(130.4 nm) and OI(135.6 nm) lines, *J. Geophys. Res. (Planets)*, 108, 5126, doi:10.1029/2004JA010798, 2003.
- Knight, S.: Parallel electric fields, *Planet. Space Sci.*, 21, 741–750, 1973.
- Kullen, A. and Janhunen, P.: Relation of polar auroral arcs to magnetotail twisting and IMF rotation: a systematic MHD simulation study, *Ann. Geophys.*, 22, 951–970, doi:10.5194/angeo-22-951-2004, 2004.
- Laher, R. R. and Gilmore, F. R.: Updated Excitation and Ionization Cross Sections for Electron Impact on Atomic Oxygen, *J. Phys. Chem. Reference Data*, 19, 277–305, 1990.
- Lassen, K. and Danielsen, C.: Quiet time pattern of auroral arcs for different directions of the interplanetary magnetic field in the Y-Z plane, *J. Geophys. Res.*, 83, 5277–5284, 1978.
- Lemaire, J. and Scherer, M.: Simple model for an ion-exosphere in an open magnetic field, *Phys. Fluids*, 14, 1683–1694, 1971.
- Lemaire, J. and Scherer, M.: Plasma sheet particle precipitation: A kinetic model, *Planet. Space Sci.*, 21, 281–289, 1973.
- Lilensten, J. and Blelly, P. L.: The TEC and F2 parameters as tracers of the ionosphere and thermosphere, *J. Atmos. Solar-Terr. Physics*, 64, 775–793, 2002.
- Lilensten, J., Kofman, W., Wisenberg, J., Oran, E. S., and Devore, C. R.: Ionization efficiency due to primary and secondary photoelectrons – A numerical model, *Ann. Geophys.*, 7, 83–90, 1989.
- Lundin, R. and Sandahl, I.: Some characteristics of the parallel electric field acceleration of electrons over discrete auroral arcs as observed from two rocket flights, Tech. Rep. SP-135, European Space Agency, 1978.
- Lyons, L. R.: Generation of large-scale regions of auroral currents,

- electric potentials and precipitation by the divergence of the convection electric field, *J. Geophys. Res.*, 85, 17–24, 1980.
- Lyons, L. R.: Discrete aurora a the direct result of an inferred high altitude generating potential distribution, *J. Geophys. Res.*, 86, 1–8, 1981.
- Lyons, L., Evans, D., and Lundin, R.: An observed relation between magnetic field-aligned electric fields and downward electron energy fluxes in the vicinity of auroral forms, *J. Geophys. Res.*, 84, 457–461, 1979.
- Maggiolo, R., Sauvaud, J. A., Fontaine, D., Teste, A., Grigorenko, E., Balogh, A., Fazakerley, A., Paschmann, G., Delcourt, D., and Rème, H.: A multi-satellite study of accelerated ionospheric ion beams above the polar cap, *Ann. Geophys.*, 24, 1665–1684, doi:10.5194/angeo-24-1665-2006, 2006.
- Maggiolo, R., Echim, M., De Keyser, J., Fontaine, D., Jacquy, C., and Dandouras, I.: Polar cap ion beams during periods of northward IMF: Cluster statistical results, *Ann. Geophys.*, 29, 771–787, doi:10.5194/angeo-29-771-2011, 2011.
- Marklund, G. T., Blomberg, L. G., Murphree, J. S., Elphinstone, R. D., and Zanetti, L. J.: On the electrodynamic state of the auroral ionosphere during northward interplanetary magnetic field – A transpolar arc case study, *J. Geophys. Res.*, 96, 9567–9578, 1991.
- Meier, R. R.: Ultraviolet spectroscopy and remote sensing of the upper atmosphere, *Space Sci. Rev.*, 58, 1–185, 1991.
- Meier, R. R., Conway, R. R., Anderson Jr., D. E., Feldman, P. D., and Gentieu, E. P.: The ultraviolet dayglow at solar maximum. III – Photoelectron-excited emissions of N<sub>2</sub> and O, *J. Geophys. Res.*, 90, 6608–6616, 1985.
- Meléndez-Alvira, D. J., Meier, R. R., Picone, J. M., Feldman, P. D., and McLaughlin, B. M.: Analysis of the oxygen nightglow measured by the Hopkins Ultraviolet Telescope: Implications for ionospheric partial radiative recombination rate coefficients, *J. Geophys. Res.*, 104, 14901–14914, 1999a.
- Meléndez-Alvira, D. J., Meier, R. R., Picone, J. M., Feldman, P. D., and McLaughlin, B. M.: Erratum: “Analysis of the oxygen nightglow measured by the Hopkins Ultraviolet Telescope: Implications for ionospheric partial radiative recombination rate coefficients”, *J. Geophys. Res.*, 104, 28215–28216, 1999b.
- Mozer, F. S., Carlson, C. W., Hudson, M. K., Torbert, R. B., Parady, B., Yatteau, J., and Kelley, M. C.: Observation of paired electrostatic shocks in the polar magnetosphere, *Phys. Rev. Lett.*, 38, 292–295, 1977.
- Murphree, J. S., Anger, C. D., and Cogger, L. L.: The instantaneous relationship between polar cap and oval auroras at times of northward interplanetary magnetic field, *Canadian J. Phys.*, 60, 349–356, 1982.
- Newell, P. T., Liou, K., and Wilson, G. R.: Polar cap particle precipitation and aurora: Review and commentary, *J. Atmos. Terrest. Phys.*, 71, 199–215, 2009.
- Paschmann, G., Quinn, J. M., Torbert, R. B., Vaith, H., McIlwain, C. E., Haerendel, G., Bauer, O. H., Bauer, T., Baumjohann, W., Fillius, W., Förster, M., Frey, S., Georgescu, E., Kerr, S. S., Kletzing, C. A., Matsui, H., Puhl-Quinn, P., and Whipple, E. C.: The Electron Drift Instrument on Cluster: overview of first results, *Ann. Geophys.*, 19, 1273–1288, doi:10.5194/angeo-19-1273-2001, 2001.
- Paxton, L. J., Christensen, A. B., Humm, D. C., Ogorzalek, B. S., Pardoe, C. T., Morrison, D., Weiss, M. B., Crain, W., Lew, P. H., Mabry, D. J., Goldsten, J. O., Gary, S. A., Persons, D. F., Harold, M. J., Alvarez, E. B., Ercol, C. J., Strickland, D. J., and Meng, C.-I.: Global ultraviolet imager (GUVID): Measuring composition and energy inputs for the NASA Thermosphere Ionosphere Mesosphere Energetics and Dynamics (TIMED) mission, *Proc. SPIE*, 3756, 265–276, 1999.
- Petrukovich, A. A., Baumjohann, W., Nakamura, R., Balogh, A., Mukai, T., Glassmeier, K.-H., Reme, H., and Klecker, B.: Plasma sheet structure during strongly northward IMF, *J. Geophys. Res.*, 108, SMP 22-1, 2003.
- Pierrard, V.: New model of magnetospheric current-voltage relationship *J. Geophys. Res.*, 101, 2669–2676, 1996.
- Rairden, R. L. and Mende, S. B.: Properties of 6300-Å auroral emissions at South Pole, *J. Geophys. Res.*, 94, 1402–1416, 1989.
- Rème, H., Aoustin, C., Bosqued, J. M., Dandouras, I., Lavraud, B., Sauvaud, J. A., Barthe, A., Bouyssou, J., Camus, Th., Coeur-Joly, O., Cros, A., Cuvilo, J., Ducay, F., Garbarowitz, Y., Medale, J. L., Penou, E., Perrier, H., Romefort, D., Rouzard, J., Vallat, C., Alcaydé, D., Jacquy, C., Mazelle, C., d’Uston, C., Möbius, E., Kistler, L. M., Crocker, K., Granoff, M., Mouikis, C., Popecki, M., Vosbury, M., Klecker, B., Hovestadt, D., Kucharek, H., Kuenneth, E., Paschmann, G., Scholer, M., Sckopke, N., Seidenschwang, E., Carlson, C. W., Curtis, D. W., Ingraham, C., Lin, R. P., McFadden, J. P., Parks, G. K., Phan, T., Formisano, V., Amata, E., Bavassano-Cattaneo, M. B., Baldetti, P., Bruno, R., Chionchio, G., Di Lellis, A., Marcucci, M. F., Pallochia, G., Korth, A., Daly, P. W., Graeve, B., Rosenbauer, H., Vasyliunas, V., McCarthy, M., Wilber, M., Eliasson, L., Lundin, R., Olsen, S., Shelley, E. G., Fuselier, S., Ghielmetti, A. G., Lennartsson, W., Escoubet, C. P., Balsiger, H., Friedel, R., Cao, J.-B., Kovrazhkin, R. A., Papamastorakis, I., Pellat, R., Scudder, J., and Sonnerup, B.: First multispacecraft ion measurements in and near the Earth’s magnetosphere with the identical Cluster ion spectrometry (CIS) experiment, *Ann. Geophys.*, 19, 1303–1354, doi:10.5194/angeo-19-1303-2001, 2001.
- Richards, P. C., Fennelly, J. A., and Torr, D. G.: EUVAC: a solar EUV flux model for aeronomic calculations., *J. Geophys. Res.*, 99, 8981–8992, 1994a.
- Richards, P. G., Fennelly, J. A., and Torr, D. G.: Erratum: “EUVAC: a solar EUV flux model for aeronomic calculations”, *J. Geophys. Res.*, 99, 13283, 1994b.
- Robinson, R. M. and Mende, S. B.: Ionization and electric field properties of auroral arcs during magnetic quiescence, *J. Geophys. Res.*, 95, 21111–21121, 1990.
- Rodriguez, J. V., Valladares, C. E., Fukui, K., and Gallagher, H. A.: Antisunward decay of polar cap arcs, *J. Geophys. Res.*, 102, 27227–27248, 1997.
- Roth, M., Evans, D., and Lemaire, J.: Theoretical structure of a magnetospheric plasma boundary: application to the formation of discrete auroral arcs, *J. Geophys. Res.*, 98, 11411–11423, 1993.
- Shue, J.-H., Chao, J. K., Fu, H. C., Russell, C. T., Song, P., Khurana, K. K., and Singer, H. J.: A new functional form to study the solar wind control of the magnetopause size and shape, *J. Geophys. Res.*, 102, 9497–9512, 1997.
- Simon, C., Lilensten, J., Moen, J., Holmes, J. M., Ogawa, Y., Okavik, K., and Denig, W. F.: TRANS4: a new coupled electron/proton transport code – comparison to observations above Svalbard using ESR, DMSP and optical measurements, *Ann.*

- Geophys., 25, 661–673, doi:10.5194/angeo-25-661-2007, 2007.
- Stone, E. J. and Zipf, E. C.: Electron-impact excitation of the 3So and 5So states of atomic oxygen, *J. Chem. Phys.*, 60, 4237–4243, 1974.
- Strickland, D. J. and Anderson Jr., D. E.: Radiation transport effects on the OI 1356-A limb intensity profile in the dayglow, *J. Geophys. Res.*, 88, 9260–9264, 1983.
- Strickland, D. J., Daniell Jr., R. E., Jasperse, J. R., and Basu, B.: Transport-theoretic model for the electron-proton-hydrogen atom aurora. 2: Model results, *J. Geophys. Res.*, 98, 21533–21548, 1993.
- Torr, M. R. and Torr, D. G.: Ionization frequencies for solar cycle 21 – Revised, *J. Geophys. Res.*, 90, 6675–6678, 1985.
- Troshichev, O. A., Gusev, M. G., Nikolashkin, S. V., and Samsonov, V. P.: Features of the polar cap aurorae in the Southern Polar Region, *Planet. Space Sci.*, 36, 429–439, 1988.
- Tsyganenko, N. A. and Sitnov, M. I.: Modeling the dynamics of the inner magnetosphere during strong geomagnetic storms, *J. Geophys. Res.*, 110, A03208, doi:10.1029/2004JA010798, 2005.
- Vaivads, A., André, M., Buchert, S., Eriksson, A. I., Olsson, A., Wahlund, J.-E., Janhunen, P., Marklund, G., Kistler, L. M., Mouikis, C., Winningham, D., Fazakerley, A., and Newell, P.: What high altitude observations tell us about the auroral acceleration: A Cluster/DMSP conjunction, *Geophys. Res. Lett.*, 30, 1106, doi:10.1029/2002GL016006, 2003.
- Valladares Jr., C. E., Carlson, H. C., and Fukui, K.: Interplanetary magnetic field dependency of stable Sun-aligned polar cap arcs, *J. Geophys. Res.*, 99, 6247–6272, 1994.
- Whalen, B. A., Miller, J. R., and McDiarmid, I. B.: Sounding Rocket Observations of Particle Precipitation in a Polar-Cap Electron Aurora, *J. Geophys. Res.*, 76, 6847–6855, 1971.
- Yau, A. W., Abe, T., and Peterson, W. K.: The polar wind: Recent observations, *J. Atmos. Terrest. Phys.*, 69, 1936–1983, 2007.
- Yoshino, K., Parkinson, W. H., Ito, K., and Matsui, T.: Absolute absorption cross-section measurements of Schumann Runge continuum of O<sub>2</sub> at 90 and 295 K, *J. Molecular Spectroscopy*, 229, 238–243, 2005.
- Zhang, Y. and Paxton, L. J.: An empirical Kp-dependent global auroral model based on TIMED/GUVI FUV data, *J. Atmos. Sol-Terr. Phys.*, 70, 1231–1242, 2008.
- Zhang, Y., Meng, C.-I., Paxton, L. J., Morrison, D., Wolven, B., Kil, H., Newell, P., Wing, S., and Christensen, A. B.: Far-ultraviolet signature of polar cusp during southward IMF Bz observed by TIMED/Global Ultraviolet Imager and DMSP, *J. Geophys. Res.*, 110, A01218, doi:10.1029/2004JA010707, 2005a.
- Zhang, Y., Paxton, L. J., Morrison, D., Lui, A. T. Y., Kil, H., Wolven, B., Meng, C.-I., and Christensen, A. B.: Undulations on the equatorward edge of the diffuse proton aurora: TIMED/GUVI observations, *J. Geophys. Res.*, 110, A08211, doi:10.1029/2004JA010668, 2005b.
- Zhang, Y., Paxton, L. J., and Lui, A. T. Y.: An unusual nightside distortion of the auroral oval: TIMED/GUVI and IMAGE/FUV observations, *J. Geophys. Res.*, 111, A08203, doi:10.1029/2005JA011217, 2006.
- Zhang, Y., Paxton, L. J., and Zheng, Y.: Interplanetary shock induced ring current auroras, *J. Geophys. Res.*, 113, A01212, doi:10.1029/2007JA012554, 2008.
- Zhang, Y., Paxton, L. J., Newell, P. T., and Meng, C.-I.: Does the polar cap disappear under an extended strong northward IMF? *J. Atmos. Sol.-Terr. Phys.*, 71, 2006–2012, 2009.
- Zhu, L., Schunk, R. W., and Sojka, J. J.: Polar cap arcs: a review, *J. Atmos. Terrest. Phys.*, 59, 1087–1126, 1997.
- Zipf, E. C. and Erdman, P. W.: Electron impact excitation of atomic oxygen – Revised cross sections, *J. Geophys. Res.*, 90, 11087–11090, 1985.